Hemmings, B., Whitaker, F., Gottsmann, J., & Hawes, M. C. (2016). Non-eruptive ice melt driven by internal heat at glaciated stratovolcanoes. *Journal of Volcanology and Geothermal Research*, *327*, 385–397. https://doi.org/10.1016/j.jvolgeores.2016.09.004

Non-eruptive ice melt driven by internal heat at glaciated stratovolcanoes

Brioch Hemmings[a,*], Fiona Whitaker[a], Joachim Gottsmann[a], Molly C. Hawes[a]

[a]*School of Earth Sciences, University of Bristol, Bristol, UK*

Abstract

Mudflows, floods and lahars from rapid snow and ice melting present potentially devastating hazards to populations surrounding glacial stratovolcanoes. Most ice-melt induced lahars have resulted from eruptive processes. However, there is evidence for non-eruptive hydrothermal volcanic unrest generating rapid and hazardous glacial melt. Here, we use TOUGH2 numerical fluid flow simulations to explore ice melt potential associated with hydrothermal perturbation. Our simulations are loosely based on Cotopaxi Volcano, Ecuadorian Andes. We show that dynamic permeability has a strong control on ice melt response to perturbation. In the absence of concurrent permeability increases, the delay time between onset of a deep hydrothermal perturbation and a response in surface heat flow is on the order of many 10s of years. When increased hot fluid influx at depth is combined with permeability enhancement, the surface heat flow response can be immediate. However, our results suggest that melt rates resulting from such hydrothermal perturbation are still orders of magnitude lower than those induced by eruptive processes; potentially hazardous melt volumes take many months to accumulate, compared to minutes for eruption induced melting. Additional mechanisms, such as glacier destabilisation, meltwater impounding and hydrothermal outburst, may be required to generate the volumes of water associated with catastrophic eruption initiated ice-melt lahars.

Keywords: volcanic unrest - glacial volcano - hydrothermal - lahar

1. Introduction

Lahars, mudflows and floods induced by ice melt are well documented in the historical and geological record. Interactions between eruptive volcanic products and glaciers have escalated

*Corresponding author
Email address: brioch.hemmings@bristol.ac.uk (Brioch Hemmings)

relatively minor volcanic eruptions into national and international disasters, with catastrophic loss of life. Although most of the documented ice-melt induced lahars have been the result of eruptive processes, there is evidence for non-eruptive hydrothermal volcanic unrest generating rapid and hazardous glacial melt. The processes that promote and control non-eruptive hydrothermal ice melting are largely unknown. Consequently, the hazard presented by non-eruptive melting at glaciated stratovolcanoes is also poorly understood.

There are a number of examples of glacial melt at ice-clad stratovolcanoes generating voluminous and catastrophic lahars. At Nevado del Ruiz, Colombia, 1985, lahars generated by a relatively small eruption (VEI= 3) produced one of the most devastating volcanic disasters in history with over 23,000 fatalities (Pierson et al., 1990). A combination of mechanical and thermal interaction between eruptive products and snow and ice generated $>1 \times 10^7\,\mathrm{m}^3$ of melt and produced a total lahar volume close to $1 \times 10^8\,\mathrm{m}^3$, with runout distances in excess of 100 km. Similar melting mechanisms have been cited as the trigger for the generation of up to 10 massive lahars in the last 800 years at Cotopaxi Volcano, Ecuador (Pistolesi et al., 2013). Worldwide the are >40 examples of volcanoes where historical eruption has perturbed snow and ice and generated lahars or floods (Major and Newhall, 1989).

The majority of lahar or flood events relating to ice melt have resulted from eruptive processes, involving the deposition of hot volcanic material directly onto the glacier (e.g. Nevado del Ruiz, 1985, Pierson et al., 1990) or related to eruption into the base of a glacier (e.g. Katla, 1918, Major and Newhall, 1989). Although limited, there is some evidence for the occurrence of non-eruptive melting resulting from hydrothermal interactions in volcanic systems. Examples range from the Aleutian Arc (e.g. Mt Spurr, 2004, Coombs et al., 2006) to Iceland (e.g. Grímsvötn, Major and Newhall, 1989), and even Mars (e.g. Craft and Lowell, 2012). Melting through such non-eruptive processes has the potential to occur without notable precursory activity. Therefore, a developing hazard associated with such melting may not be recognised in volcanic monitoring data. Here, we use TOUGH2 (specifically, iTOUGH2, V6.6) fluid flow simulations to assess the potential for the generation of significant rates and volumes of ice melt from non-eruptive hydrothermal perturbations at glaciated stratovolcanoes. We explore the controls on the spatial and temporal response of surface heat flux to changes within an idealised, active hydrothermal system.

2. Methods and model development

We develop simulations of hydrothermal flow beneath a high relief stratovolcano. Model geometry is based on a topographic profile for Cotopaxi stratovolcano, Ecuador (Jordan et al., 2005). The models are not designed to describe or predict the behaviour of Cotopaxi Volcano in detail but aim to explore, more generally, the viability of potential hydrothermal unrest scenarios producing rapid and volumous ice melt. This allows a generalised investigation of the processes and features that control surface heat flux at restless, ice-clad stratovolcanoes.

2.1. Initial model

The *Initial* model is two-dimensional (2-D) and axisymmetric about $x = 0$ m, where the central crater is at elevation $z = 5600$ m (Figure 1). The model extends laterally to $x = 6000$ m, where the top surface is at $z = 4150$ m. In this initial model, isotropic permeability is defined as a function of depth, d, after Saar and Manga (2004) and Manning and Ingebritsen (1999):

$$k_d = \begin{cases} k_0 e^{-\lambda d} & \text{for } 0 \leq z \leq 800 \text{ m} \\ k_{800} \frac{d}{800}^{-3.2} & \text{for } z > 800 \text{ m}\,, \end{cases} \tag{1}$$

where k is permeability in m^2, at depth d in m; k_0 is the surface permeability ($5 \times 10^{-13}\,\mathrm{m}^2$); k_{800} is the permeability at $d = 800$ m according to the upper equation in Equation 1, and $\lambda = 0.004$.

As our main focus is on the behaviour of the convective regime, we place the base on the model at $z = 3000$ m (Figure 1). At this depth the permeability over the majority of the model base is less than $10^{-16}\,\mathrm{m}^2$, which is often considered to be the lower limit for effective heat advection (e.g. Norton and Knight, 1977; Ingebritsen and Hayba, 1994). Focussing on the upper 3 km of the edifice also makes it easier to keep the simulations within the subcritical limitation of the TOUGH2 version used. For water the critical point occurs at ∼22 MPa and ∼374 °C (Jupp and Schultz, 2000). At near-critical and supercritical conditions heat transport may be greatly enhanced (Ingebritsen and Hayba, 1994; Coumou et al., 2008). Although, supercritical-capable adaptations of TOUGH2 codes have been developed (Croucher and O'Sullivan, 2008), the version of the code used here (iTOUGH2 V6.6) does not have fluid property definitions above the critical point and simulations will stop if such conditions develop. This thermodynamic limitation does restrict the model scenarios that can be explored, particularly in magmatic hydrothermal systems. However, in a number of simulations using the supercritical-capable HYDROTHERM simulator to explore controls on groundwater and

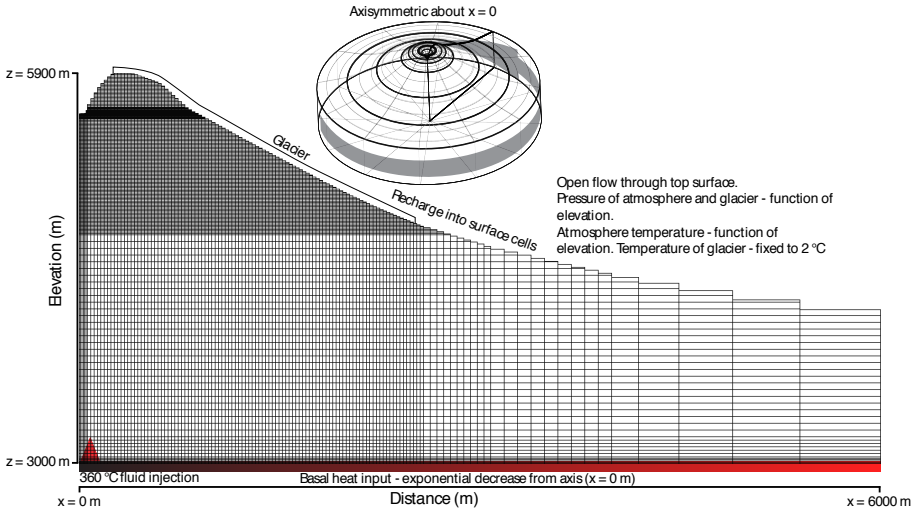

Figure 1: *Initial* model geometry, showing rectilinear mesh division and boundary conditions

heat transport in magmatic hydrothermal systems, Hurwitz et al. (2003) did not produce supercritical conditions in the upper 3 km of a geometrically similar domain. In numerical simulations of fluid flow behaviour around magmatic intrusions using Complex Systems Modeling Platform (CSMP++), Scott et al. (2015) found that supercritical conditions were generally limited to a thin boundary region around the intrusion. There is value in investigating the behaviour of subcritical systems and the responses to potential subcritical perturbations. Subcritical flow represent the less extreme, less dynamic flow regimes of a hydrothermal system, especially in terms of efficiency of energy transfer. However, if subcritical hydrothermal flow can generate surface heat flux capable of precipitating hazardous ice melt, it is reasonable to expect that perturbation of a hydrothermal system that produces more pervasive supercritical flow would also result in significant ice melt on glaciated stratovolcanoes.

In this *Initial* model both the axial and distal lateral boundaries are closed to flow. Due to the 2-D axisymmetric geometry the most distal cells have very large volumes ($\sim 1.07 \times 10^9\,\mathrm{m}^3$). Additional simulations (not shown) have demonstrated that there is little difference between simulations where the distal boundary is maintained at initial hydrostatic pressure and temperature conditions and opened to flow, and where the distal boundary is closed to flow. The basal boundary is also closed to flow but all basal cells act as heat sources, with additional fluid generation in basal cells within $x < 150$ m. (Figure 1). Heat generation rate (q_H, in $\mathrm{W\,m}^{-2}$) is defined to logarith-

mically decrease, from q_{H1}= 2.0 W m^{-2} at the axial boundary (x_1 = 5 m) to q_{H2}= 0.24 W m^{-2} at x_2 = 10000 m, according to the relationship:

$$q_H = a \ln(bx)\,, \tag{2}$$

$$\text{where,} \qquad a = \frac{q_{H1} - q_{H2}}{\ln(x_1/x_2)}$$

$$\text{and} \qquad b = e^{\frac{q_{H2}\ln(x_1) - q_{H1}\ln(x_2)}{q_{H1} - q_{H2}}}$$

The total heat generation in the base of the model domain is ∼53 MW. This is within the heat input range used by Hurwitz et al. (2003) (14 – 62 MW). To represent an influx of hydrothermal fluid, water with a temperature of 360 °C is injected at a rate of 1×10^{-3} kg s^{-1} m^{-2} into basal cells where $x < 150$ m. The phase of the injected fluid is determined by the thermodynamic conditions in the injection cells. The total basal injection rate is ∼80 kg s^{-1}. For comparison, Hurwitz et al. (2003) injected 550 °C fluid at a much lower rate of 0.09 kg s^{-1} and at a greater depth (∼5 km).

The glacier covers the region at the top surface boundary for $250 < x < 2500$ m (Figure 1). The glacier is considered warm-based and therefore sufficiently connected with the atmosphere to justify defining the ground surface boundary as gas-filled and at atmospheric pressure. Flow is permitted through this boundary and the atmospheric pressure, in Pa, is fixed as a function of elevation:

$$P = 1.01 \times 10^5 (1 - 2.26 \times 10^{-5} z)^{5.26}\,, \tag{3}$$

where z is elevation in metres. The temperature at the top boundary (°C) is also fixed. Outside the glaciated region, surface temperature follows an approximate lapse rate for the tropical Andes (e.g. Bradley et al., 2009):

$$T = 25.8 - \frac{5.4z}{1000}\,. \tag{4}$$

The lower temperature limit supported by the iTOUGH2 V6.6 code is 1 °C. To prevent our simulations from dropping below this level we impose surface temperature lower limit of 2 °C. Recharge is applied in all the surface cells. Rates of subglacial recharge to groundwater are relatively underconstrained; in high elevation environments such as the volcanic edifices of the Ecuadorian Andes, even precipitation rates can exhibit great spatial variability (Vuille et al., 2000). Monthly data presented by Veettil et al. (2014) provides an annual precipitation estimate of ∼1100 mm for Cotopaxi

volcano. This is comparable with the estimate of 1020 mm yr^{-1} at 4650 m elevation at nearby Antizana Volcano (Favier et al., 2008). However, other authors have estimated that annual precipitation may reach 6000 mm at the peaks of the Ecuadorian Andes (Garreaud, 2009). Through observations and mass balance calculations, Favier et al. (2008) estimate that groundwater recharge from the glacier at Antizana occurs at a rate of 100 – 900 mm yr^{-1}. Here we use a recharge rate equivalent to 500 mm yr^{-1} at a temperature defined by Equation 4 but constrained within the 2°C lower limit.

The 2-D axisymmetric domain is divided into a rectilinear mesh of columns and rows (Figure 1). Row thicknesses vary between 2 and 50 m. In order to optimise the resolution at the surface, especially in the crater region and beneath the glacier, the thinnest rows are in the upper 1300 m, and column widths increase with distance from the $x = 0$ m axis, from 10 to 600 m. To improve the resolution around the fluid and heat injection cells the row thickness is also reduced to 10 m near the basal boundary. The total number of cells in the model is 13,379.

Under fully saturated initial conditions, the early stages of the simulation is occupied with model drainage to establish a water table. The final water table elevation is essentially a product of balancing recharge and gravitational groundwater out-flow. Such drainage can be computationally intensive as it requires many phase changes as cells transition from single-phase (water saturated) to two-phase conditions. To reduce the simulation runtime spent with this routine but computationally expensive activity, and based on the saturation conditions that develop in preliminary simulations, we specify initial fully saturated conditions below $z = 4800$ m and two-phase conditions above (liquid saturation, $S_l = 0.7$).

2.1.1. Initial model results

The *Initial* model produces a two-phase plume. However, the upward propagation of hot fluid is completely suppressed by the cool topographic recharge and surface heat flux is low (Figure 2). Preliminary simulations that perturb this system for 1000 years failed to alter the surface heat flux and produce any additional glacial melt. Perturbation of such a suppressed initial system seems unlikely to produce hazardous levels of glacial melt. This result is consistent with simulations presented by Hurwitz et al. (2003) in which the ascent of a hydrothermal plume requires the presence of moderate permeability pathways extending to depth. To investigate the potential for rapid response of surface heat flux to perturbation it is important to explore the perturbation of a system that is closer to a critical threshold.

Even during periods of relative quiescence at the ice-capped Cotopaxi Volcano, the crater region is ice-free, with temperatures ∼50 °C (e.g. Instituto Geofísico, 2015). Within the limitation of subcritical fluid conditions, we develop this *Initial* model to explore potential mechanisms for generating crater heat flow, and therefore elevated temperature and an ice-free crater. We then explore effects of perturbation of these models on surface heat flux and potential ice melt.

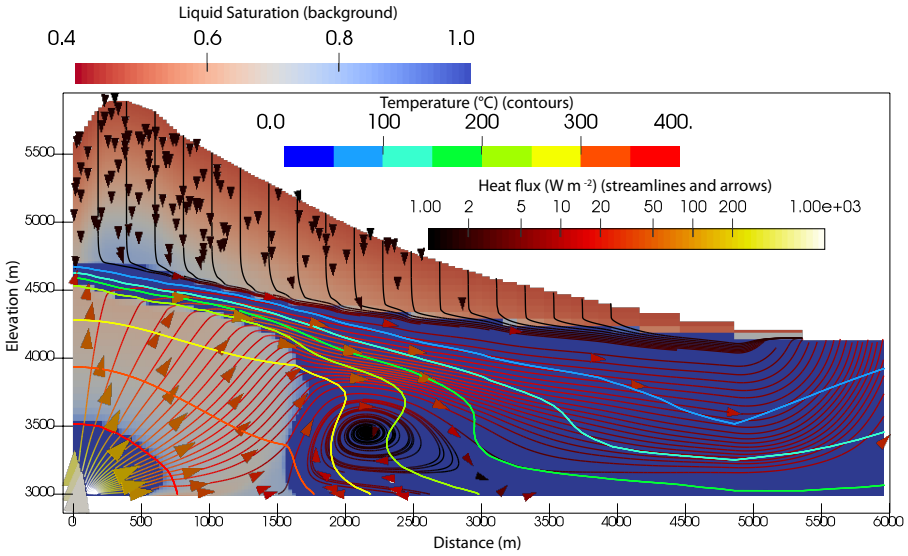

Figure 2: Liquid saturation (background colours), temperature (coloured contours), and heat flux (stream lines and arrows) at the end of the *Initial* model simulation (3500 years). Note logarithmic scale for heat flux.

2.2. Crater heat flow

We simulate two major model scenarios that are variations of the *Initial* model, described above. The first is the addition of a region of high vertical permeability (k_z) beneath the crater, referred to herein as the high permeability conduit (*HPC*). This scenario is modelled using the same 2-D axisymmetric geometry as the *Initial* model. The second scenario is modelled with a 2-D linear geometry and is designed to explore flow within the plane of a high permeability fault or fracture network; we refer to this model as fault flow (*FF*) simulation.

In the *HPC* models, we explore two different permeability modifications, relative to the *Initial* model (Figure 3). In *HPC1*, the vertical permeability (k_z) is increased by one order of magnitude in the region close to the axial boundary, beneath the crater (where $x < 250$ m). This represents

the fractured and damaged conduit that allows gasses and steam to escape from the volcano. In *HPC2*, horizontal permeability (k_x) is also increased by an order of magnitude in the uppermost portion of the edifice (where $z > 5250$ m), representing younger, less consolidated volcanic deposits.

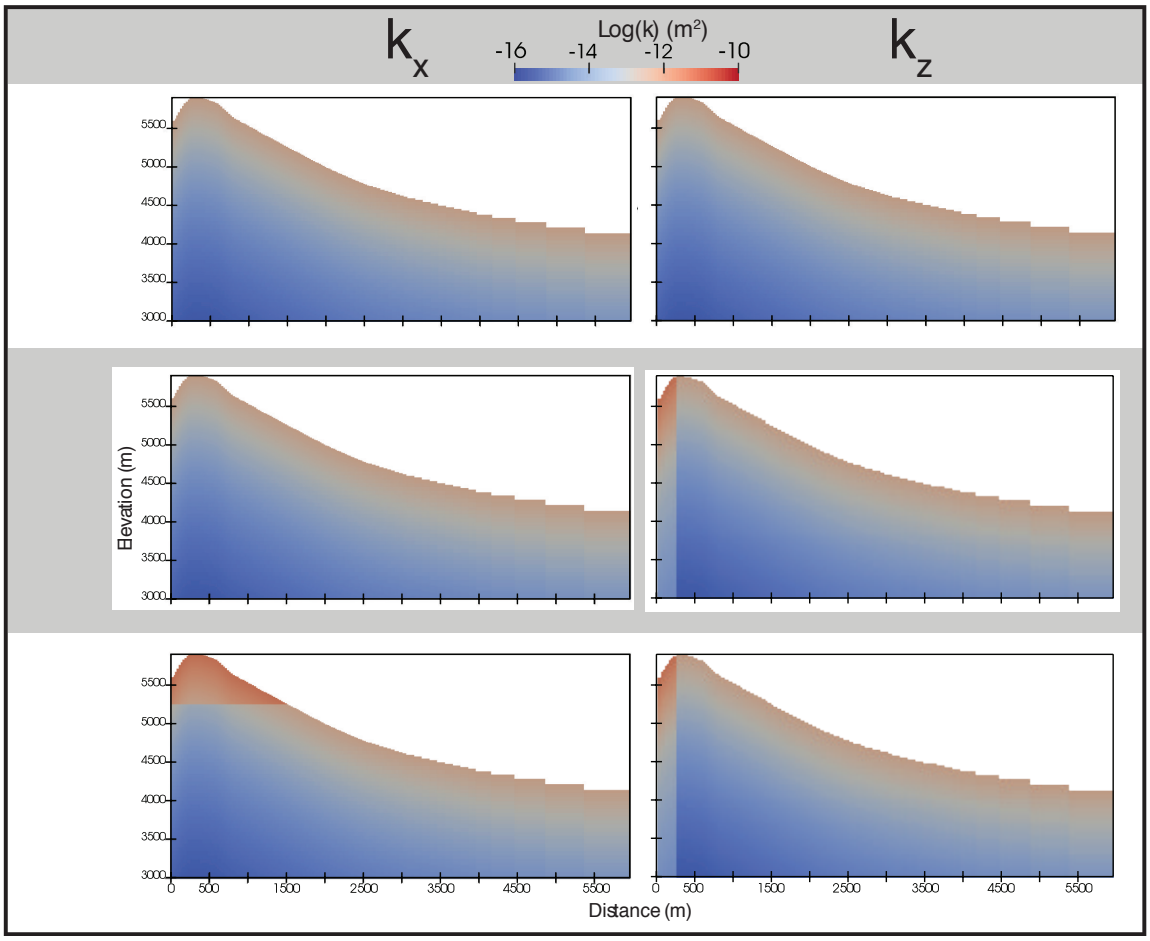

Figure 3: Horizontal (k_x) and vertical (k_z) permeability variations for *HPC* models, compared to the *Initial* model.

For the *FF* simulation the isotropic permeability is increased by a factor of 10, compared to *Initial* model. In these linear 2-D models the distal boundary is open to flow and water saturated. The pressure of these distal boundary cells is fixed to hydrostatic and the temperature follows a geothermal gradient of 12.5 °C per 100 m from a surface temperature of 2.4 °C, which is consistant with Equation 4.

In all *HPC* and *FF* simulations the permeability and depth relationship defined by Equation 1

is maintained. The surface recharge conditions also remain consistent with the *Initial* model. The *Initial* model approaches supercritical conditions at the base of the model. To reduce likelihood of the *HPC* and *FF* simulations achieving supercritical conditions, heat and fluid generation rates at the basal boundary are modified. q_{H1} in Equation 2 is reduced to $1\,\mathrm{W\,m^{-2}}$. Fluid injection flux is also halved to $0.5 \times 10^{-3}\,\mathrm{kg\,s^{-1}\,m^{-2}}$ where $x < 150$ m at the basal boundary (Table 1).

Table 1: Basal boundary conditions in simulations. Injection is at an enthalpy equivalent to 360 °C.

Simulation	Injection rate $\mathrm{kg\,s^{-1}\,m^{-2}}$	Injection region	q_{H1} (Equation 2) $\mathrm{W\,m^{-2}}$
Initial	$1{\times}10^{-3}$	$x < 150$ m	2
HPC, *FF*	$0.5{\times}10^{-3}$	$x < 150$ m	1

The simulations are allowed to run to numerical steady-state which is defined as 10 consecutive time-steps where convergence criteria are met without update of primary thermodynamic variables (Pruess et al., 1999). Where a boiling front progresses slowly or stagnates, the simulation can become numerically unstable as cells on the edge of boiling regions switch between single- and two-phase conditions. This instability can lead to simulations terminating before "steady-state" is achieved. Early termination occurs in both *HPC* models (after 4680 yr for *HPC1* and 6613 yr for *HPC2*). However, the changes in the conditions (pressure, temperature, saturation) within the domain are minimal between the time-steps prior to termination. Any changes are constrained at depth to the periphery of the rising two-phase plume; the surface heat flux has stabilised. The linear 2-D simulation *FF* does achieve steady-state, after 7151 yr.

2.3. Perturbation

The final conditions for *HPC* and *FF* models are used as initial conditions for models simulating volcanic or hydrothermal perturbations, summarised in Table 2. Perturbation scenarios include increases in thermal fluid influx and heat input at the model base (Simulations *HPC-A* to *HPC-C* and *FF-A* to *FF-D*) to instantaneous permeability increases (Simulations *HPC-D* and *FF-E*). Basal fluid and heat flux increases may reflect rupturing of a hydrothermal seal releasing pressurised hydrothermal fluids into the shallower edifice, similar to a model presented by Fournier (1999). In *HPC-C* and *HPC-D* we incorporate a shallow injection source along the axial boundary at depth $4500 < z < 5000$. This may represent break-out of hydrothermal fluids to shallower depths

along flow pathways. Similar break-out behaviour has been observed in petroleum hydrofracture operations (e.g. Sharma et al., 2004). Five-fold permeability increases are combined with increased basal influx in *HPC-D* and *FF-E*, reflecting permeability enhancements associated with fracture opening to the surface. In *HPC-D* the permeability increases are concentrated within the high permeability conduit ($x < 250$ m). We run the perturbed simulations for 1000 years. We assess the changes in surface heat flux and from this infer the changes in basal melt rate of the glacier. Clearly, a hydrothermal system within an active volcano will be modified by eruption or ongoing dynamic behaviour of the volcano. Although some volcanoes do exhibit long repose periods before eruptions, on the order of millennia (e.g. Santiaguito, Guatemala; Bezymianny, Russia), 1000 years is well beyond the eruption return period for most active volcanoes (Sheldrake et al., 2016). Our choice of 1000 year perturbation is somewhat arbitrary and we will focus on the response in the first 200 years.

2.4. Melt conversion

Modelled surface heat fluxes in $\mathrm{W\,m^{-2}}$ are converted to ice melt rates by dividing by the enthalpy of fusion for water at 1 atmosphere pressure ($3.34 \times 10^5\,\mathrm{J\,kg^{-1}}$). This gives melt rates in $\mathrm{kg\,s^{-1}\,m^{-2}}$ or $\mathrm{mm\,s^{-1}}$, which, with knowledge of the glacial area affected, can be converted to melt volumes per unit time ($\mathrm{m^3\,min^{-1}}$ or $\mathrm{m^3\,yr^{-1}}$).

3. Results

3.1. Steady-state scenarios

The introduction of a high permeability region at the axial boundary beneath the crater generates a significant increase in the heat flux into the crater, compared to the *Initial* simulation (see Figures 4 and 5, and Table 3). At the end of the *HPC1* and *HPC2* simulations, assumed to be steady-state, the total heat output through the crater (Q_{crat}) is 2.6×10^6 and 1.4×10^6 W, respectively, compared to 5.8×10^2 W for the *Initial* model (Table 3). The modification of the permeability distribution, compared to the *Initial* simulations, only has a minor effect on the heat flow to the base of the glacier ($250 < x < 2500$ m, Q_{glac}, Table 3).

The 2-D linear steady-state model, *FF* also generates heat flow into the crater (Figure 6). The reduced surface area for the linear model, compared to *HPC* models, results in lower total crater flow ($\mathrm{Q}_{crat} = 4.2 \times 10^3$ W). However, the heat flux per unit area into the crater (q_{crat}) is comparable;

Table 2: Perturbation scenarios explored in simulations. 'Injection rate' refers to the mass injection of ∼360 °C fluid close to the basal boundary within the region defined in the 'Injection region' column. *HPC-A* and *HPC-B* scenarios also include increases in basal heat input which is defined by the logarithmic relationship in Equation 2 with an increase in the heat flux at the axial boundary (q_{H1}, at $x = 0$ m). The total heat flow into the domain is provided for reference. Additional perturbations include injection of hot fluid at the axial boundary between $4500 < z < 5000$ m (denoted by 'a' in the final column) and increases in permeability (k) ('b' and 'c' in the final column).

Simulation	Injection rate ($\mathrm{kg\,s^{-1}\,m^{-2}}$)	Injection region	q_{H1} (Eq. 2) ($\mathrm{W\,m^{-2}}$)	Total heat input (MW)	
HPC	0.5×10^{-3}	$x < 150$ m	1.0	38	
HPC-A	1.0×10^{-3}	$x < 150$ m	2.0	53	
HPC-B	2.0×10^{-3}	$x < 150$ m	2.0	53	
HPC-C	1.0×10^{-3}	$x < 150$ m	1.0	38	a
HPC-D	1.0×10^{-3}	$x < 150$ m	1.0	38	a , b
FF	0.5×10^{-3}	$x < 150$ m	1.0	2×10^{-3}	
FF-A	1.0×10^{-3}	$x < 150$ m	1.0	2×10^{-3}	
FF-B	1.0×10^{-3}	$x < 300$ m	1.0	2×10^{-3}	
FF-C	2.0×10^{-3}	$x < 150$ m	1.0	2×10^{-3}	
FF-D	2.0×10^{-3}	$x < 300$ m	1.0	2×10^{-3}	
FF-E	2.0×10^{-3}	$x < 300$ m	1.0	2×10^{-3}	c

[a] Injection of ∼360 °C fluid at $0.5 \times 10^{-3}\,\mathrm{kg\,s^{-1}\,m^{-2}}$, at axial boundary, in the region $4500 < z < 5000$ m

[b] Permeability enhancement of $k \times 5$ in region $x < 250$ m

[c] Permeability enhancement of $k \times 5$ throughout

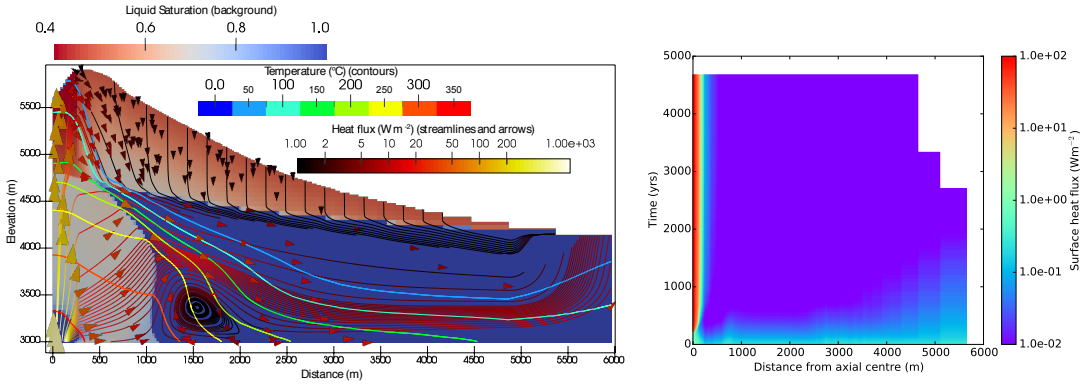

(a) (b)

Figure 4: *HPC1* simulation results. (a) Liquid saturation (background colours), temperature (coloured contours), and heat flux (stream lines and arrows). (b) Spatial and temporal distributions of surface heat flux; note logarithmic scale. White regions indicate the absence of outward surface heat flux.

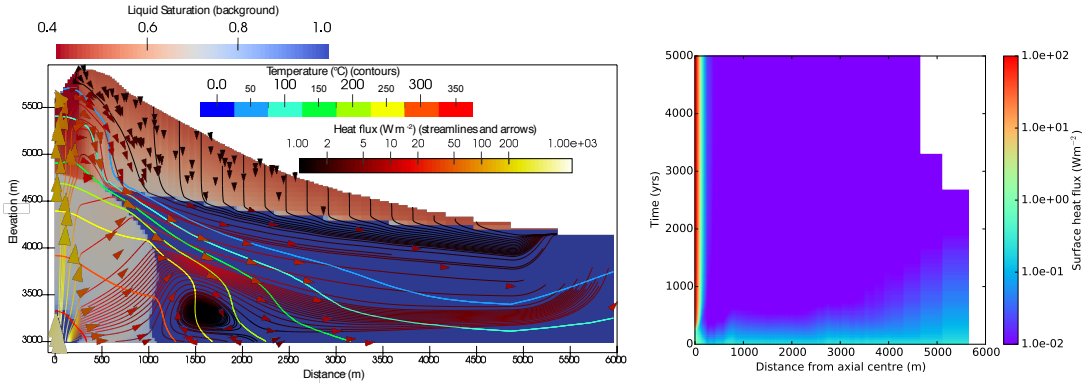

(a) (b)

Figure 5: *HPC2* simulation results. (a) Liquid saturation (background colours), temperature (coloured contours), and heat flux (stream lines and arrows). (b) Spatial and temporal distributions of surface heat flux; note logarithmic scale. White regions indicate the absence of outward surface heat flux.

Table 3: Steady-state heat flow (Q) and heat flux (q) to crater (subscript $_{crat}$) and glacier (subscript $_{glac}$), and estimated glacial melt rate (M).

Simulation	*Initial*	*HPC1*	*HPC2*	*FF*
Q_{crat} (W)	5.84×10^{2}	2.61×10^{6}	1.37×10^{6}	4.23×10^{3}
q_{crat} (W m^{-2})	2.97×10^{-3}	13.3	6.98	16.9
Q_{glac} (W)	5.48×10^{4}	7.81×10^{4}	6.79×10^{4}	2.40×10^{4}
q_{glac} (W m^{-2})	2.80×10^{-3}	3.99×10^{-3}	3.47×10^{-3}	10.7
M (m^{3} yr^{-1})	5181	7388	6418	2270

17 W m^{-2} for *FF*, and 13 and 7 W m^{-2} for *HPC1* and *HPC2*, respectively. This simulation also produces heat flux into the base of the glacier (q_{glac}) at $250 < x < 2500$ m. The average flux into the glacier of ~10 W m^{-2} produces an estimated melt rate of <1 m yr^{-1}.

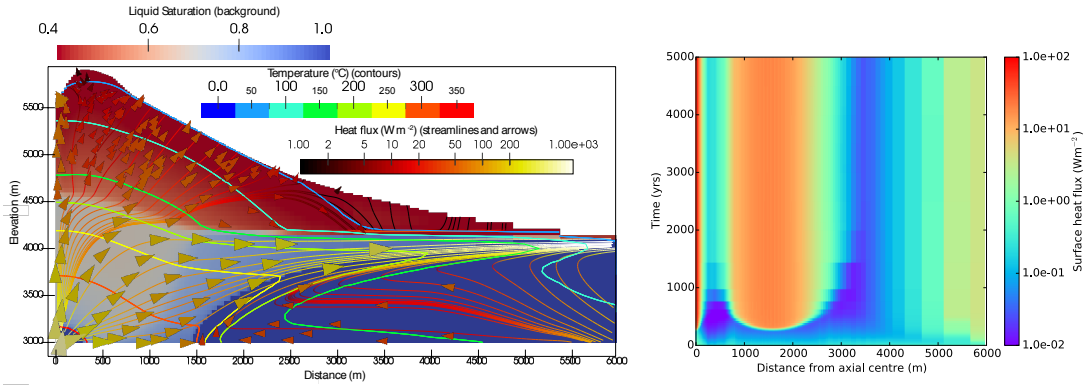

(a) (b)

Figure 6: *FF* simulation results. (a) Liquid saturation (background colours), temperature (coloured contours), and heat flux (stream lines and arrows). (b) Spatial and temporal distribution of surface heat flux; note logarithmic scale.

3.2. Perturbation scenarios

All of the perturbation scenarios presented in Table 2 result in an increase in surface heat flux beneath the glacier ($250 \leq x \leq 2500$ m) within 1000 years (See Figures A.1 to A.3). Figures 7 to 9 show the distribution of surface heat flux into the base of the glacier and the evolution of heat into

the glacier for the initial 200 years of simulated perturbation. Also displayed (green lines in right-hand plots of Figures 7 to 9 and A.1 to A.3) is time evolution of average heat flux into the glacier, relative to the contact area between the glacier and model domain. For the 2-D axisymmetric models (*HPC1* and *HPC2*) this glacial contact area is 19.44 km^2. For the 1 m wide, 2-D linear *FF* models the glacial contact area is just 2250 m^2. Figures A.4 to A.6 show the evolution of the modelled heat flux to the crater and glacier regions combined, for each perturbation scenario in Table 2.

3.2.1. HPC perturbation

As with the steady-state *HPC* simulations, the majority of the surface heat flow in the perturbed *HPC* simulations is into the crater region ($x < 250$ m) (Figures A.4 to A.5). The changes in heat flux into the base of the glacier occur close to the crater, at the inner edge of the glacier (see a,c,e,g in Figures 7 and 8). In all of the *HPC* perturbation scenarios there is a significant delay from onset of the perturbation (at time = 0) to the increase in the heat flux into the glacier.

Scenario *HPC-A* produces only a minor increase in flux into the glacier after 150 years, for *HPC1* (Figures 7a,b). For *HPC2* this perturbation scenario produces no clear surface flux increase into the glacier within 200 years (Figures 8a,b). Perturbation scenario *HPC-B* has the highest basal injection rate of all of the *HPC* simulations and also the highest heat injection flux. This scenario results in supercritical conditions at the base and the simulations stopped after 135 years for *HPC1-B* and after 138 years for *HPC2-B*. Scenarios *HPC-C* and *HPC-D* incorporate a shallower injection of hot fluid in the region $4500 < z < 5000$ m at the axial boundary. However, there is still limited appreciable increase (>10%) in heat flux into the glacier within 80 years for *HPC1-C* (Figures 7e,f) and 150 years for *HPC2-C* (Figures 8e,f). Perturbation scenario *HPC-D* also includes an instantaneous five-fold permeability increase beneath the crater region, in the central conduit ($x < 250$ m). This scenario produces the most rapid response of heat flux into the glacier. Heat flow into the glacier increases rapidly after a delay of ∼10 years and ∼30 years, for *HPC1* and *HPC2*, respectively (Figures 7g,h and 8g,h).

Although the results for *HPC1* and *HPC2* perturbation simulations are similar (compare Figure A.1 and Figure A.2), the delay for surface heat flux response is greater for *HPC2* models (Table 4). These have higher horizontal permeability in the upper part of the modelled edifice (see Figure 3). Despite the greater delay time for surface heat flux response in the *HPC2* simulations, where

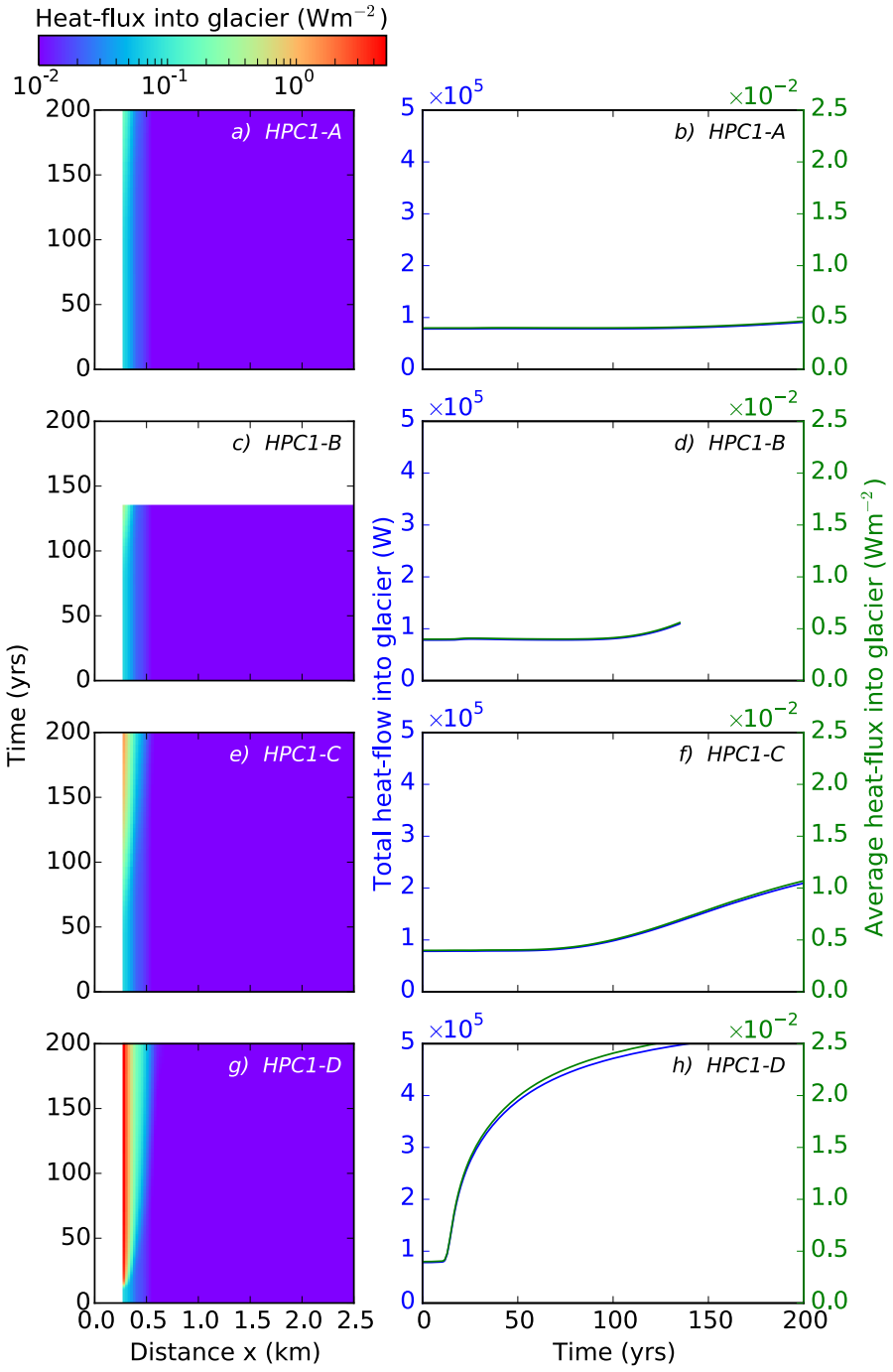

Figure 7: *HPC1* perturbation results for first 200 yrs of simulation time. Left-hand plots (a,c,e,g) show temporal and spatial variation in heat flux into glacier ($250 < x < 2500$ m); note logarithmic colour scale. Right-hand plots (b,d,f,h) show time series of total heat flow and average heat flux to glacier. The results for the full 1000 years of perturbation are presented in Figure A.1.

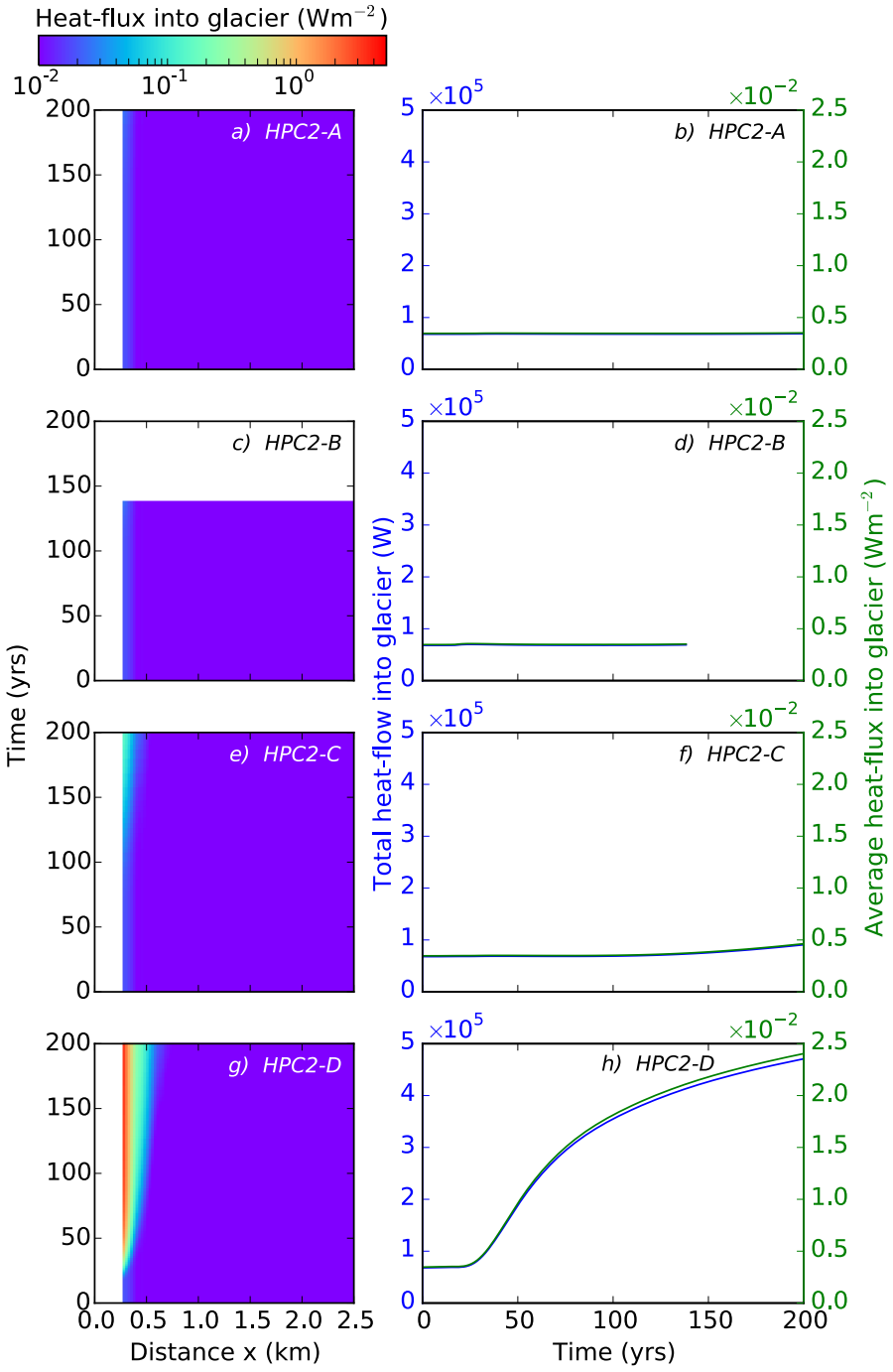

Figure 8: *HPC2* perturbation results for first 200 yrs of simulation time. Left-hand plots (a,c,e,g) show temporal and spatial variation in heat flux into glacier ($250 < x < 2500$ m); note logarithmic colour scale. Right-hand plots (b,d,f,h) show time series of total heat flow and average heat flux to glacier. The results for the full 1000 years of perturbation are presented in Figure A.2.

243 the perturbation scenarios include shallow fluid injection (*HPC-C* and *HPC-D*), the final heat flow
244 into the glacier (after 1000 years) is higher than in the equivalent *HPC1* scenario.

Table 4: Delay time for heat flow into the glacier base to increase by a factor of 2, 4 and 10, compared to initial (steady-state) heat flow. Crosses indicate that the heat flow to the glacier did not increase by that factor during the 1000 year simulation.

	Heat flow into glacier, relative to steady-state		
Simulation	×2	×4	×10
HPC1-A	414 yr	x	x
HPC1-B	x	x	x
HPC1-C	151 yr	422 yr	x
HPC1-D	16 yr	31 yr	x
HPC2-A	x	x	x
HPC2-B	x	x	x
HPC2-C	300 yr	570 yr	x
HPC2-D	40 yr	68 yr	x
FF-A	100 yr	x	x
FF-B	68 yr	77 yr	x
FF-C	68 yr	77yr	x
FF-D	45 yr	46 yr	52 yr
FF-E	0.3 yr	1 yr	15 yr

245 *3.2.2. FF perturbation*

246 All of the perturbation scenarios produce a marked increase in heat flux into the base of the
247 glacier (Figure 9) and apparent steady surface heat flux conditions within 150 years of the per-
248 turbation onset (at time = 0). As with the steady-state simulations, the reduced glacial surface
249 contact area in these 2-D linear models (compared to the *HPC* 2-D axisymmetric models) results
250 in lower total modelled heat flow into the base of the glacier. However, the heat flux per unit of
251 glacial contact area is significantly higher.

252 In contrast to the 2-D axisymmetric (*HPC1*) models, the highest heat flux to the glacier in

the 2-D linear fault (*FF*) simulations is through the flanks of the modelled edifice, away from the crater (Figures 9a,c,e,g,i, note scale change). The heat flux increase also occurs more rapidly than for the majority of the *HPC* models (Table 4). Scenarios *FF-A* to *FF-D* explore variations in the basal fluid injection rate and injection area. Generally, the magnitude of the perturbation increases from *FF-A* to *FF-D* (Table 2). The amplitude of the flux increase scales with the magnitude of the perturbation. The onset time for surface flux increase scales inversely with the magnitude of perturbation (Table 4). For *FF-C* the injection rate is double that of *FF-B*, but the injection area is half (see Table 2). The surface heat flux results for these two scenarios are very similar (Figures 9c,d and 9e,f). Perturbation scenario *FF-E* differs from *FF-D* in that it includes an immediate five-fold permeability enhancement. This scenario produces an immediate increase in heat flux into the glacier. It also produces the highest heat flux per unit of glacial contact area of all the scenarios ($\sim$200 W m^{-2}) and has the shortest time-delay between perturbation initiation and maximum surface heat flux ($\sim$ 35 years).

3.3. Melt rates

The maximum heat flux to the glacier produced by all of these simulations is 320 W m^{-2}, in *FF-D* and *FF-E*. This equates to $\sim$83 mm d^{-1} loss rate from the base of the glacier and would result in a $\sim$30 m reduction in thickness in a year. The peak total ice melt at 37 years for simulation *FF-E* is $\sim$118 m^3 d^{-1} (4.3×10^4 m^3 yr^{-1}). Despite the time lag, simulation *HPC2-D* produces the highest peak melt rate, approximately 175 m^3 d^{-1} (6.4×10^4 m^3 yr^{-1}) at the end of the 1000 year perturbation.

3.4. Water table stability and formation of crater lakes

In the *Inital* model simulation the upward propagation of hot fluid is suppressed by cool recharging groundwater. Similarly, the downward flow of cool recharging water is inhibited by the rising two-phase plume. A saturated perched aquifer is generated above the rising plume, supplied from above by recharging groundwater, and from below by condensing steam (Figure 2). Perching of the liquid saturated region is maintained by a combination of fluid pressure balance in the two regions and relative permeability contrasts between the single-phase liquid-saturated region above, and the two-phase region below.

The stability of the perched saturated zone is a function of complex feedbacks between the intrinsic permeability, relative permeability with respect to different phases, and the pressure and

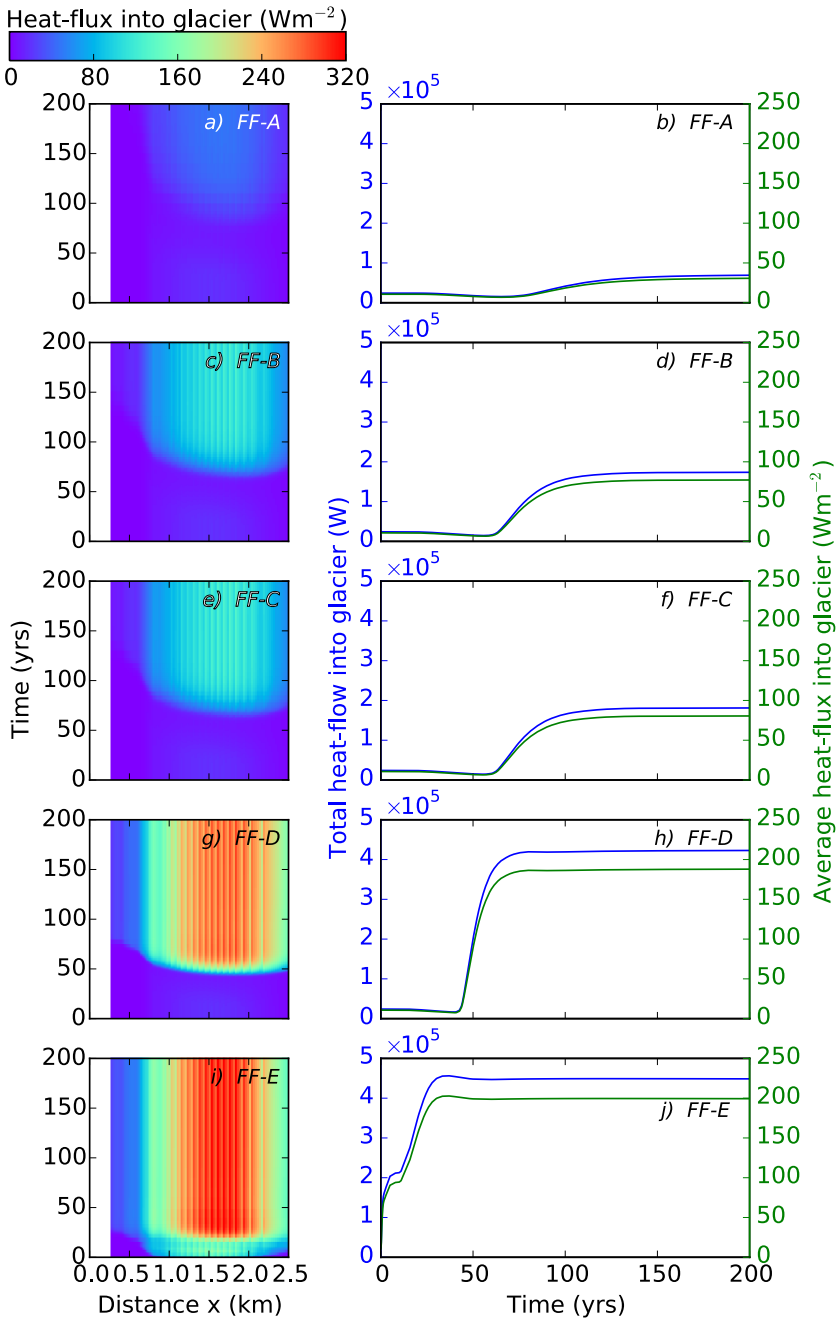

Figure 9: *FF* perturbation results for first 200 yrs of simulation time. Left-hand plots (a,c,e,g,i) show temporal and spatial variation in heat flux into glacier ($250 < x < 2500$ m); note colour scale change compared to Figures 7 and 8. Right-hand plots (b,d,f,h,j) show time series of total heat flow and average heat flux to glacier; note change in secondary y-axis scale compared to Figures 7 and 8. The results for the full 1000 years of perturbation are presented in Figure A.3.

temperature conditions. In the *Initial* model (Figure 2) the conditions support a relatively stable perched saturated region. Many of the simulations demonstrate more dynamic and unstable perched saturation conditions in response to thermodynamic changes associated with the model perturbations. An example of this for simulation *FF-D* is illustrated in Figure 10.

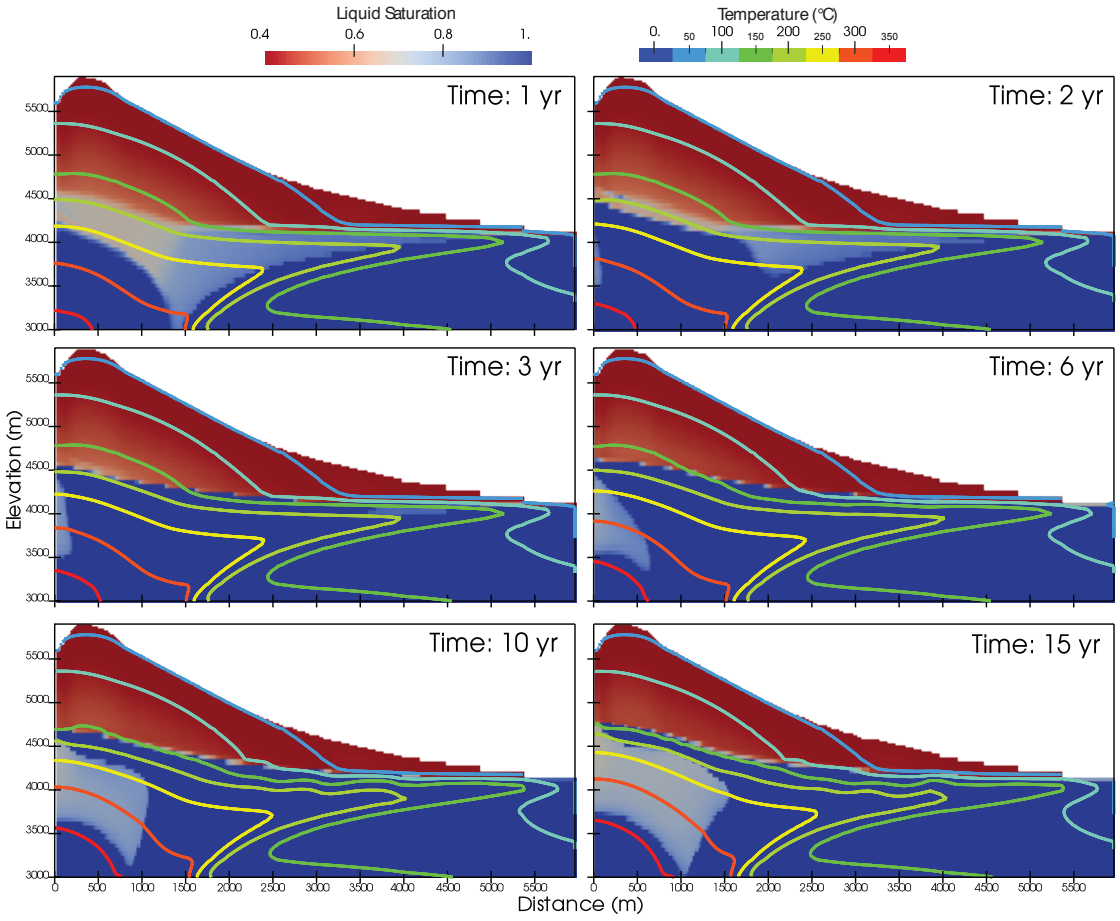

Figure 10: Development of a dynamic perched water table in perturbation simulation *FF-D*. The initial state, prior to perturbation, is presented in Figure 6a.

In *FF-D* the increase in pressure associated with the increased injection rate (see Table 2) causes the two-phase plume to condense. Within two years, this results in >200 °C liquid saturated conditions at 4500 m elevation. Over the following 8 years, the thermal effects of the perturbation propagate upwards from the injection site, a two-phase region is re-established, the elevation of

the water table increases by ∼300 m, and the temperature at the water table drops to ∼150 °C. The two-phase plume eventually pushes through the perched saturated region in the inner 300 m of the domain. However, a saturated zone persists at an elevation of 5000 m with temperatures between 130 and 200 °C until ∼30 years after the onset of the perturbation. We observe this dynamic water-table behaviour at different spatial and temporal scales in most of our perturbation simulations. These additional observations may provide insights into the dynamics of crater lakes and hydrothermal outflow at restless volcanoes. Such behaviour also has implications for volcanic edifice stability. Saturation and pore-fluid temperature increases can elevate pore pressures above failure thresholds and can trigger deep-seated gravitational collapse (Reid, 2004).

4. Discussion

4.1. Controls on surface heat flow

The steady-state models demonstrate the importance of permeability structures in controlling the spatial distribution of fluid and heat flow within the edifice. Consequently, permeability also controls the spatial distribution of surface heat flux. Without the presence of permeability contrasts, specifically high permeability flow pathways, cool recharge waters can suppress the upward propagation of thermal waters. We demonstrate two mechanisms for producing surface heat flow into a summit crater with subcritical fluid injection and basal heat input 2.5 km beneath the surface: i) flow up a high permeability central conduit (*HPC*). ii) flow within the plane of a fault or fracture network (*FF*)

The total heat flow into the crater (Q_{crat}) is strongly affected by the distribution of subsurface permeability structures. Unfortunately, there is a paucity of heat flow observations from Cotopaxi or other low-latitude Andean glaciated volcanoes for direct comparison of modelled crater heat flow. However, some heat flow estimates do exist from glaciated volcanoes elsewhere in the world (e.g. Mount Rainier, Cascades, USA; Frank, 1995). Frank (1995) report total heat flow of 8.6 MW in the the crater at Mount Rainier. The highest value for Q_{crat} produced by the steady-state models is 2.6 MW in simulation *HPC1*. However, averaged over the whole crater area of the model, $Q_{crat} = 2.6$ MW represents a flux (q_{crat}) of ∼13 W m^{-2}. This is comparable with the area average crater heat flux of 16 W m^{-2} observed at Mount Rainier which has a larger crater area. Frank (1995) reported localised thermal areas within the Mount Rainier crater with a surface heat flux of

$700\,\mathrm{W\,m^{-2}}$. The nature of our model discretisation and relatively coarse parameterisation means that the simulations presented here will not resolve small scale flow features that might be associated with such large but localised fluxes. Whilst the simulated crater heat flux is reasonable, it is probable that finer scale permeability features control the finer detail of surface heat flux distribution.

The models in this study do not explore the fluid and heat transport scenarios associated with supercritical fluid conditions. Enhanced heat transfer has been shown to occur at near-critical conditions as fluid enthalpy and density change rapidly around the critical point. Dunn and Hardee (1981) observe heat transfer rates increase by a factor of 70 close to the critical point and dubbed the process "superconvection". Using numerical simulations Ingebritsen and Hayba (1994) suggest that near the critical point, heat transfer enhancements greater than a factor of 100 may occur. However, they highlight that such superconvection also requires high permeabilities, on the order of 10^{-13} $\mathrm{m^2}$. In high strain rate environments, permeable pathways may be maintained to depth, against competing factors such as silica deposition (Ingebritsen and Hayba, 1994). In geothermal reservoirs permeabilities between 1×10^{-15} and $1 \times 10^{-13}\,\mathrm{m^2}$ are often reported (Björnsson and Bodvarsson, 1990); so superconvection may play a role in the environments explored in this study. However, in a recent study Scott et al. (2016) explore the structure and behaviour of supercritical geothermal systems in response to shallow magmatic intrusions into the upper 3km of a saturated, flat topographic domain. In their models, supercritical conditions are confined to regions immediately adjacent to the modelled intrusion. Our model results, at least qualitatively, are consistent with their general conclusions; in low permeability systems ($1 \times 10^{-16}\,\mathrm{m^2}$) plume development is inhibited, similar to our *Initial* simulation, while at intermediate permeabilities ($1 \times 10^{-15}\,\mathrm{m^2}$), equivalent to our *HPC* simulation, boiling zones can extend to the surface. Magmatic intrusion to shallower depths may promote supercritical (or superheated, after Scott et al., 2015) fluid conditions within higher permeability units nearer the surface. However, in high permeability systems, supercritical flow is confined to ~10 m boundary around the intrusion (Scott et al., 2015). In the case of a shallow intrusion, even if subcritical flow dominates, one would expect higher surface heat flow and reduced perturbation response delay time compared to the scenarios investigated here. The results from *HPC-C* and *HPC-D* scenarios suggest that, although the inclusion of shallow perturbation does increase net surface heat flow as well as reduce the delay time, the spatial distribution of surface heat flow, and therefore the effect on an ice-cap in our model geometry, is largely controlled by the permeability distribution.

In all of the *HPC* perturbation models, surface heat flux changes occur predominantly within the crater region above the higher permeability central core. The presence of higher horizontal permeability in the uppermost region of the *HPC2* simulations further delays the surface heat flux response, compared to the *HPC1* simulations. The high horizontal permeability reduces the focussing of hot fluid upwards towards the crater, and promotes lateral flow into the shallow portion of the edifice where the thermal fluids mix with cool recharging groundwater. This reduces the heat outflow in the crater region and the inner portion of the glacier. For perturbation scenarios with shallow injection of hot fluids (*HPC-C* and *HPC-D*), the increased horizontal permeability in *HPC2* eventually produces higher total heat flow into the glacier. However, the delay time for the increase in surface heat flow is greater than for the equivalent *HPC1* scenarios.

The delay between the initiation of perturbation and an increase in surface heat flux is significant. There is a lag of 50 years for most of the perturbation scenarios. Long lag-times mean that enhanced glacial melt from these perturbation scenarios is unlikely to present an immediate additional hazard in dynamic volcanic hydrothermal systems. On these timescales, such changes in the state and extent of the glacier may be difficult to differentiate from effects of a changing climate (Huggel et al., 2007). Shorter lag-times are produced by perturbation scenarios with permeability enhancements (*HPC-D* and *FF-E*). Scenario *FF-E* is the only simulation that produces an immediate increase in heat flow to the glacier; heat flow to the glacier triples within 6 months, and there is a ten-fold heat flow increase within 18 months.

The *HPC* perturbation scenarios with a permeability enhancement (*HPC-D* simulations) show a slower increase in heat flow to the glacier than *FF-E*. For these simulations, permeability increase is confined to the region beneath the crater ($x < 250$ m) and not the subsurface below the glacier. The location of the glacier on the flank of the volcano means that it is isolated from surface heat flux increases which are focused into the crater region by the high permeabilities in the central conduit (Figures A.4g and A.5g). In contrast, there is a ten-fold increase in heat flow into the crater within 3 years. Heat flow to the crater peaks after about 7 years at values of 84 MW and 60 MW for *HPC1-D* and *HPC2-D*, respectively. However, the lag time for a 10% increase in heat flow to the glacier is 12 and 26 years, for *HPC1-D* and *HPC2-D*, respectively.

These results highlight that the existing intrinsic permeability structures are important for controlling the movement of fluid, transport of heat towards the surface, and the spatial distribution of surface heat flow. Furthermore, permeability changes within a complex and dynamic active

volcanic edifice can have a dramatic effect on both the spatial and temporal behaviour of surface heat flux. Such changes in permeability, termed dynamic permeability (Gessner et al., 2009), can result from chemical and physical interactions between fluids and rocks, rock deformation from local and regional stresses, and also from the interaction between competing fluid phases within the hydrothermal system. These processes can occur over timescales ranging from minutes (e.g. rapid hydrofracturing, Miller and Nur 2000; earthquake induced changes, Rojstaczer and Wolf 1992) to many years (e.g. hydrothermal alteration, precipitation of mineral veins, Dobson et al. 2003). The magnitude, ubiquity and timescales of these dynamic permeability processes, and their effect on fluid flow at active volcanoes, requires continued investigation. For example, in the enhanced permeability perturbation simulations presented here (*FF-E* and *HPC-D*), we specify that the magnitude of the permeability increase is five-fold. This enhancement occurs in regions where the permeability is already enhanced ten-fold above the 'background permeability' (in the central conduit in *HPC* simulations and throughout the domain in the *FF* model). Therefore, the net increase above the 'background permeability' is fifty-fold. There is some evidence for local permeability enhancements on the order of 100- to 200-fold in enhanced/engineered geothermal systems (e.g. Evans et al., 2005). However, Evans et al. (2005) also suggest that net or area averaged enhancements may only be on the order of fifteen-fold. The presence of fumaroles on active volcanoes is indicative of localised enhanced permeability flow pathways. The simulations here, particularly *HPC* simulations, do not capture these fine scale features. However, as is indicated by *FF* simulations, their location in relation to glacial cover may be important in dictating melt rate and glacial stability. If permeability enhancements of many orders of magnitude are achieved, one might expect even more rapid surface heat flow responses and possibly even rapid decompression (and boiling) of a shallow hydrothermal system.

4.2. Melt volumes and hazards

Comparison between modelled glacial melt rates and observed melt rates of mountain glaciers is non-trivial. Glacial melt rates are variously reported as area loss (in m^2); percentage area change; mass balance deficit, balancing precipitation input and melting (in $m\,yr^{-1}$); or even ice-line elevation change (in m). The fluid flow models here provide estimates for ice melt mass (in kg) or melt volume (in m^3). A rare estimate of quiescent period ice volume loss from Nevado del Huila, Colombia, is $\sim 1 \times 10^7\,m^3\,yr^{-1}$ ($\sim 19\,m^3\,min^{-1}$) (Huggel et al., 2007). The glacier at Nevado del Huila, with a

summit elevation of 5365 m, has a similar areal extent to the glacier of Cotopaxi. It is unclear if this estimated ice volume loss relates to net loss of ice or the annual melt volume discharged to the drainage channels. Water equivalent melt rates of 3-4 $\mathrm{m\,yr^{-1}}$ have been proposed for the Cotopaxi glacier (Jordan et al., 2005). The peak volume melt rate for *FF-E* is just $4.3 \times 10^4\,\mathrm{m^3\,yr^{-1}}$ ($0.08\,\mathrm{m^3\,min^{-1}}$). This melt rate is small compared to the probable total background ice loss from the entire glacier. However, the ice loss is derived from a relatively small area of the glacier (2250 $\mathrm{m^2}$). The total melt rate by volume is clearly a function of the contact area between with the glacier and the sites of surface heat flow. It is likely that the width of a fault-bounded flow system is greater than the 1 m defined in the *FF* model geometry. The total melt volume would be expected to scale with this width. A melt rate of $4.3 \times 10^4\,\mathrm{m^3\,yr^{-1}}$ ($0.08\,\mathrm{m^3\,min^{-1}}$) over 2250 $\mathrm{m^2}$ contact area equates to average thickness loss of $19\,\mathrm{m\,yr^{-1}}$, over this area. The modelled melt rate in scenario *FF-E* would result in removal of 30 m of ice, from the glacial area that is in contact with the model, within 3 years.

The localised melting produced by the *FF* model geometry would likely focus melt water into relatively few drainage channels, potentially overwhelming the carrying capacity of the glacial streams. Such localised melting may also destabilise portions of the glacier and produce glacial mass failures. Such mass failures are thought to have contributed to the generation of catastrophic eruptive lahars at Nevado del Ruiz in 1985 (Pierson et al., 1990). However, even accounting for potentially larger contact areas than were modelled by *FF* simulations, the melt rates generated by the models presented here are many orders of magnitude lower than those estimated from Nevado del Ruiz. Pierson et al. (1990) estimate that melt volumes from passive deposition of hot pyroclastic material at Nevado del Ruiz could account for a total melt volume of over $7 \times 10^5\,\mathrm{m^3}$ within just 10 minutes ($\sim 7 \times 10^4\,\mathrm{m^3\,min^{-1}}$). Owing to processes such as thermal and mechanical erosion from the transit of pyroclastic flows, the total volume of water within the initial lahars is estimated to be closer to $3 \times 10^7\,\mathrm{m^3}$. By comparison, the maximum melt rate produced by the models presented here is just $0.12\,\mathrm{m^3\,min^{-1}}$, after a thousand year delay from the onset of the perturbation. The response is more rapid for *FF-E*, however, at $\sim 0.08\,\mathrm{m^3\,min^{-1}}$, the melt rates are even lower. In the models presented here, loosely based on high elevation, low latitude stratovolcanoes like Cotopaxi, the crater area is assumed to be ice free. Our results demonstrate that when assessing the threat posed by glacial melting due to hydrothermal perturbation, the spatial relationship between ice and snow coverage and sub-subsurface permeability structures is critical. If we lift the ice free crater assumption in

HPC1-D the focusing of surface heat flux within the crater region by the permeability distribution (Figure A.4g) results in a maximum glacial melt rate of $15\,m^3\,min^{-1}$.

Although we cannot fully assess the potential role of supercritical fluid flow on surface heat flux and ice melt rate, from the limited scenarios tested here it seems unlikely that non-eruptive basal melting could generate sufficient melt to produce catastrophic Nevado del Ruiz-scale lahars. Even if the glacial contact width for simulation *FF-E* was 50 m, it would take 3-6 months before the melt volume reached $1 \times 10^5\,m^3$; a volume that may be sufficient to initiate a significant lahar. Although such melt rates will increase the run-off down glacial drainage channels and may result in water level rises downstream, they are unlikely to generate hazardous lahars. However, if the melt water is suddenly released after being impounded on the flanks by rock or ice barriers, it could generate a significant lahar. This is the basic mechanism behind jökulhlaups (glacial lake outbursts), a relatively common feature of volcanism beneath Icelandic glaciers (e.g. Björnsson, 2003). Due to less favourable glacier geometries, there are fewer examples of glacial meltwater outbursts from glaciated peaks of stratovolcanoes, although some do exist (e.g. Villarrica, Chile in 1971, reported in Major and Newhall, 1989). The presence of a crater in our model geometry does present an opportunity to impound large volumes of melt water in a crater lake. Under the glaciated crater assumption, briefly discussed above as applied to *HPC1-D*, $1 \times 10^5\,m^3$ of meltwater could be accumulated within 1 month and $7 \times 10^5\,m^3$ after 6 months. Sudden release of melt water accumulated in the crater region would have the potential to precipitate a hazardous lahar.

Aside from melt water ponding and glacier mass collapse (ice-slides), there are other glacial, geomechanical and hydrological interactions that could result in enhanced melting and high volumes of water flow on volcano flanks. These include hydrothermal outflow directly into the base of the glacier, and rapid release from a pressurised shallow geothermal aquifer. These scenarios have not been explicitly simulated by the numerical simulation presented here. However, we have presented additional observations of dynamic water-table fluctuations that may provide insights into hydrothermal outflow behaviour and crater lake dynamics, as well as have implications for edifice stability.

A number of our simulations produce a saturated region, suspended above a rising two-phase plume (e.g. Figure 6a). The appearance and position of such a saturated zone, and its dissipation, are sensitive to changes in the hydrothermal system. Our models simulate very large >300 m changes in water-table elevation in response to hydrothermal perturbation scenarios (e.g. Figure

10). The combination of edifice geometry, permeability, recharge rate, and hydrothermal conditions in our simulations ensure that the elevation of the water-table remains ∼1 km below the surface. However, it is conceivable that under alternative hydrogeological and hydrothermal conditions these dynamic fluctuations in the water-table elevation could occur close to the surface. Where water-table fluctuations intersect the base of a volcanic crater this behaviour might result in the appearance and disappearance of a crater lake. A similar perching mechanism has been suggested to explain dynamic behaviour at Boiling Lake, Dominica (Fournier et al., 2009). If the water-table is close to the ground-surface on the flanks of a volcano, water-table elevation fluctuations could result in hydrothermal outflow. Such outflow events were observed prior to the 1902 eruption at Mount Pelée (Tanguy, 1994).

The location of hydrothermal outflow is closely connected to fault features; specifically, areas of interacting active fracturing (Curewitz and Karson, 1997). The importance of these permeability features is highlighted by our modelling results. Imaging and mapping potential fracture pathways and, if possible, regions of heightened heat flux beneath glaciers is critical for accurate assessment of the hazard presented by non-eruptive ice melt. High-resolution location of seismic swarms may help to illuminate the migration of hydrothermal fluid and identify potential permeability-enhancing events. This information should be incorporated into more detailed fluid flow models to explore more volcano-specific unrest scenarios.

5. Conclusions

In the suite of fluid flow models presented here we explore the potential for hydrothermally initiated ice melt at glacial stratovolcanoes. We have demonstrated that hydrothermal perturbation can increase surface heat flux and thus also increase ice melt. However, simulated total melt rates remain low, compared to melt rates associated with documented glacial lahars. Therefore, our results suggest that hydrothermal unrest alone is unlikely to precipitate catastrophic lahars at glaciated stratovolcanoes.

Simulations presented here highlight the importance of existing permeability structures in controlling the location of surface heat flux and demonstrate that dynamic permeability changes can significantly alter the spatial and temporal response of surface heat flux to volcanic and hydrothermal unrest. We explore two permeability distribution scenarios: a central high permeability conduit within a 2-D axisymmetric domain (HPC), and a 2-D linear high permeability fault or fracture zone

(*FF*). Steady-state simulations demonstrate that permeable flow pathways facilitate surface heat flux by connecting the volcanic hydrothermal system to the surface. The location and properties of these permeable pathways exerts a strong control on the spatial distribution of surface heat flux.

In order to address the potential for hazardous ice melt from non-eruptive volcanic unrest, we explore a number of hydrothermal perturbation scenarios and assess the temporal and spatial surface heat flow response. We particularly focus on the heat flow to a glacier on the flank of the volcano. Generally, the response of surface heat flux to hydrothermal perturbation is slow. For *HPC* simulations, in the absence of an additional permeability enhancement, increased thermal fluid injection at depth fails to produce an appreciable increase in surface heat flux within 50 years. Even with a simultaneous shallow injection of 360°C fluid, a noticeable surface heat flux increase is delayed by 35 years. The surface heat flux is concentrated in the crater region of the model domain, above the high permeability conduit. Increase in heat flow to the base of the glacier is delayed by ∼100 years from the onset of the perturbation.

Simulations of hydrothermal perturbation that include instantaneous permeability enhancements generate a much more rapid surface heat flux response. A permeability increase of half an order of magnitude in the central conduit of the *HPC* model produces a rapid increase in surface heat flux. However, the surface heat flux increase is largely confined to the region above the central conduit; there is still a 10-25 year delay before an increase in heat flux into the base of the glacier which is located on the flank of the modelled volcano. The ice melt potential of a particular surface heat flux increase is strongly controlled by the relative locations of the glacier, and regions of enhanced surface heat flow which are a product of the sub-surface permeability distribution. A five-fold permeability increase in a 2-D linear fault-bounded model domain (*FF*) results in an immediate increase in heat flow to the glacier base. However, the time required to melt volumes of ice required for lahar initiation ($\sim 10^5\,\mathrm{m}^3$) is on the order of many months.

We discuss some potential mechanisms that could combine with non-eruptive hydrothermally induced melting to generate volumes of water on the order required to produce potentially hazardous lahars ($10^5\,\mathrm{m}^3$). Suggested processes include; glacial instability and collapse, associated with focussing of surface heat flux; hydrothermal outpouring, related to near surface water table dynamics in response to hydrothermal perturbation; and impounding of melt water by geometrical interaction between glacier and volcano surface morphology. Based on the results presented here, we suggest that a combined historical, field, analogue and numerical investigation of these

mechanism is warranted. We also recommend identification and monitoring of preferential subsurface flow pathways, regions of heightened surface heat flux, and glacial discharge water at ice-clad stratovolcanoes that pose a flood or lahar hazard to nearby communities.

Acknowledgments

This work was supported by the European Commission's 7th Framework Programme under contract #282759 "VUELCO". Thanks are due to Adrian Croucher (University of Auckland) for developing pyTOUGH and promptly responding to questions and edit requests; to Stefan Finsterle (Lawrence Berkeley National Laboratory) for his patient support relating to TOUGH2. The authors are also grateful to Nico Fournier and a second anonymous reviewer for detailed and constructive reviews that have helped us to improve the manuscript significantly.

References

Björnsson, G., Bodvarsson, G., 1990. A survey of geothermal reservoir properties. Geothermics 19, 17–27. doi:10.1016/0375-6505(90)90063-H.

Björnsson, H., 2003. Subglacial lakes and jökulhlaups in Iceland. Glob. Planet. Change 35, 255–271. doi:10.1016/S0921-8181(02)00130-3.

Bradley, R.S., Keimig, F.T., Diaz, H.F., Hardy, D.R., 2009. Recent changes in freezing level heights in the Tropics with implications for the deglacierization of high mountain regions. Geophys. Res. Lett. 36, L17701. doi:10.1029/2009GL037712.

Coombs, M.L., Neal, C.A., Wessels, R.L., McGimsey, R.G., 2006. Geothermal disruption of summit glaciers at Mount Spurr Volcano, 2004-6: An unusual manifestation of volcanic unrest. U.S. Geol. Surv. Prof. Pap. 1732-B , 1–33.

Coumou, D., Driesner, T., Heinrich, C.A., 2008. Heat transport at boiling, near-critical conditions. Geofluids 8, 208–215. doi:10.1111/j.1468-8123.2008.00218.x.

Craft, K.L., Lowell, R.P., 2012. Boundary layer models of hydrothermal circulation on Mars and its relationship to geomorphic features. J. Geophys. Res. E Planets 117, 1–16. doi:10.1029/2012JE004049.

Croucher, A.E., O'Sullivan, M.J., 2008. Application of the computer code TOUGH2 to the simulation of supercritical conditions in geothermal systems. Geothermics 37, 622–634. doi:10.1016/j.geothermics.2008.03.005.

Curewitz, D., Karson, J.a., 1997. Structural settings of hydrothermal outflow: Fracture permeability maintained by fault propagation and interaction. J. Volcanol. Geotherm. Res. 79, 149–168. doi:10.1016/S0377-0273(97)00027-9.

Dobson, P., Kneafsey, T., Hulen, J., Simmons, A., 2003. Porosity, permeability, and fluid flow in the Yellowstone geothermal system, Wyoming. J. Volcanol. Geotherm. Res. 123, 313–324. doi:10.1016/S0377-0273(03)00039-8.

Dunn, J., Hardee, H., 1981. Superconvecting geothermal zones. J. Volcanol. Geotherm. Res. 11, 189–201. doi:10.1016/0377-0273(81)90022-6.

572 Evans, K.F., Genter, A., Sausse, J., 2005. Permeability creation and damage due to massive fluid
573 injections into granite at 3.5 km at Soultz: 1. Borehole observations. J. Geophys. Res. Solid
574 Earth 110, 1–14. doi:10.1029/2004JB003168.

575 Favier, V., Coudrain, A., Cadier, E., Francou, B., Ayabaca, E., Maisincho, L., Praderio, E., Villacis,
576 M., Wagnon, P., 2008. Evidence of groundwater flow on Antizana ice-covered volcano, Ecuador
577 / Mise en évidence d'écoulements souterrains sur le volcan englacé Antizana, Equateur. Hydrol.
578 Sci. J. 53, 278–291. doi:10.1623/hysj.53.1.278.

579 Fournier, N., Witham, F., Moreau-Fournier, M., Bardou, L., 2009. Boiling Lake of Dominica,
580 West Indies: High-temperature volcanic crater lake dynamics. J. Geophys. Res. 114, B02203.
581 doi:10.1029/2008JB005773.

582 Fournier, R., 1999. Hydrothermal processes related to movement of fluid from plastic into brittle
583 rock in the magmatic-epithermal environment. Econ. Geol. 94.

584 Frank, D., 1995. Surficial extent and conceptual model of hydrothermal system at Mount Rainier,
585 Washington. J. Volcanol. Geotherm. Res. 65, 51–80. doi:10.1016/0377-0273(94)00081-Q.

586 Garreaud, R.D., 2009. The Andes climate and weather. Adv. Geosci. 22, 3–11. doi:10.5194/adgeo-
587 22-3-2009.

588 Gessner, K., Kühn, M., Rath, V., Kosack, C., Blumenthal, M., Clauser, C., 2009. Coupled Process
589 Models as a Tool for Analysing Hydrothermal Systems. Surv. Geophys. 30, 133–162. doi:10.
590 1007/s10712-009-9067-1.

591 Huggel, C., Ceballos, J.L., Pulgarin, B., Ramirez, J., 2007. Review and reassessment of haz-
592 ards owing to volcano glacier interactions in Colombia. Ann. Glaciol. , 128–136doi:10.3189/
593 172756407782282408.

594 Hurwitz, S., Kipp, K., Ingebritsen, S., Reid, M.E., 2003. Groundwater flow, heat transport, and
595 water table position within volcanic edifices: Implications for volcanic processes in the Cascade
596 Range. J. Geophys. Res. 108, 2557. doi:10.1029/2003JB002565.

597 Ingebritsen, S., Hayba, D.O., 1994. Fluid flow and heat transport near the critical point of H 2 O.
598 Geophys. Res. Lett. 21, 2199–2202. doi:10.1029/94GL02002.

599 Ingebritsen, S., Shelly, D.R., Hsieh, P.A., Clor, L.E., Seward, P.H., Evans, W.C., 2015. Hydrother-
600 mal response to a volcano-tectonic earthquake swarm, Lassen, California. Geophys. Res. Lett.
601 42, 9223–9230. doi:10.1002/2015GL065826.

602 Instituto Geofísico, 2015. Resumen de las observaciones efectuadas durante el vuelo al Volcán
603 Cotopaxi del dia 18 de Agosto de 2015. URL: http://www.igepn.edu.ec/servicios/
604 noticias/1144-resumen-de-las-observaciones-efectuadas-durante-el-vuelo-al-
605 volcan-cotopaxi-del-dia-18-de-agosto-de-2015.

606 Jordan, E., Ungerechts, L., Cáceres, B., Peñafiel, A., Francou, B., 2005. Estimation by pho-
607 togrammetry of the glacier recession on the Cotopaxi Volcano (Ecuador) between 1956 and 1997
608 / Estimation par photogrammétrie de la récession glaciaire sur le Volcan Cotopaxi (Equateur)
609 entre 1956 et 1997. Hydrol. Sci. J. 50, 949–962. doi:10.1623/hysj.2005.50.6.949.

610 Jupp, T., Schultz, a., 2000. A thermodynamic explanation for black smoker temperatures. Nature
611 403, 880–3. doi:10.1038/35002552.

612 Major, J.J., Newhall, C., 1989. Snow and ice perturbation during historical volcanic eruptions and
613 the formation of lahars and floods. Bull. Volcanol. 52, 1–27. doi:10.1007/BF00641384.

614 Manning, C., Ingebritsen, S., 1999. Permeability of the continental crust: Implications of geothermal
615 data and metamorphic systems. Rev. Geophys. .

616 Miller, S.a., Nur, A., 2000. Permeability as a toggle switch in fluid-controlled crustal processes.
617 Earth Planet. Sci. Lett. 183, 133–146. doi:10.1016/S0012-821X(00)00263-6.

618 Norton, D., Knight, J., 1977. Transport phenomena in hydrothermal systems: cooling plutons. Am.
619 J. Sci.;(United States) 277.

620 Pierson, T.C., Janda, R.J., Thouret, J.C., Borrero, C.a., 1990. Perturbation and melting of
621 snow and ice by the 13 November 1985 eruption of Nevado del Ruiz, Colombia, and con-
622 sequent mobilization, flow and deposition of lahars. J. Volcanol. Geotherm. Res. 41, 17–66.
623 doi:10.1016/0377-0273(90)90082-Q.

624 Pistolesi, M., Cioni, R., Rosi, M., Cashman, K.V., Rossotti, A., Aguilera, E., 2013. Evidence
625 for lahar-triggering mechanisms in complex stratigraphic sequences: the post-twelfth century

626 eruptive activity of Cotopaxi Volcano, Ecuador. Bull. Volcanol. 75, 698. doi:10.1007/s00445-
627 013-0698-1.

628 Pruess, K., Moridis, G., Oldenburg, C., 1999. TOUGH2 user's guide, version 2.0. Technical Report
629 November. Lawrence Berkeley National Laboratory. Berkeley, CA.

630 Reid, M.E., 2004. Massive collapse of volcano edifices triggered by hydrothermal pressurization.
631 Geology 32, 373. doi:10.1130/G20300.1.

632 Rojstaczer, S., Wolf, S., 1992. Permeability changes associated with large earthquakes: An exam-
633 ple from Loma Prieta, California. Geology 20, 211. doi:10.1130/0091-7613(1992)020<0211:
634 PCAWLE>2.3.CO;2.

635 Saar, M.O., Manga, M., 2004. Depth dependence of permeability in the Oregon Cascades inferred
636 from hydrogeologic, thermal, seismic, and magmatic modeling constraints. J. Geophys. Res. 109,
637 B04204. doi:10.1029/2003JB002855.

638 Scott, S., Driesner, T., Weis, P., 2015. Geologic controls on supercritical geothermal resources above
639 magmatic intrusions. Nat. Commun. 6, 7837. doi:10.1038/ncomms8837.

640 Scott, S., Driesner, T., Weis, P., 2016. The thermal structure and temporal evolution of high-
641 enthalpy geothermal systems. Geothermics 62, 33–47. doi:10.1016/j.geothermics.2016.02.
642 004.

643 Sharma, M.M., Gadde, P.B., Sullivan, R., Sigal, R., Fielder, R., Copeland, D., Griffin, L., Weijers,
644 L., 2004. Slick Water and Hybrid Fracs in the Bossier: Some Lessons Learnt, in: SPE Annu.
645 Tech. Conf. Exhib., Society of Petroleum Engineers. pp. 26–29. URL: http://www.onepetro.
646 org/doi/10.2118/89876-MS, doi:10.2118/89876-MS.

647 Sheldrake, T., Sparks, R., Cashman, K., Wadge, G., Aspinall, W., 2016. Similarities and
648 differences in the historical records of lava dome-building volcanoes: Implications for un-
649 derstanding magmatic processes and eruption forecasting. Earth-Science Rev. 160, 240–263.
650 doi:10.1016/j.earscirev.2016.07.013.

651 Tanguy, J.C., 1994. The 1902-1905 eruptions of Montagne Pelée, Martinique: anatomy and retro-
652 spection. J. Volcanol. Geotherm. Res. 60, 87–107. doi:10.1016/0377-0273(94)90064-7.

Veettil, B.K., Leandro Bayer Maier, É., Bremer, U.F., de Souza, S.F., 2014. Combined influence of PDO and ENSO on northern Andean glaciers: a case study on the Cotopaxi ice-covered volcano, Ecuador. Clim. Dyn. 43, 3439–3448. doi:10.1007/s00382-014-2114-8.

Vuille, M., Bradley, R.S., Keimig, F., 2000. Climate Variability in the Andes of Ecuador and Its Relation to Tropical Pacific and Atlantic Sea Surface Temperature Anomalies. J. Clim. 13, 2520–2535. doi:10.1175/1520-0442(2000)013<2520:CVITAO>2.0.CO;2.

A. Supplementary Figures

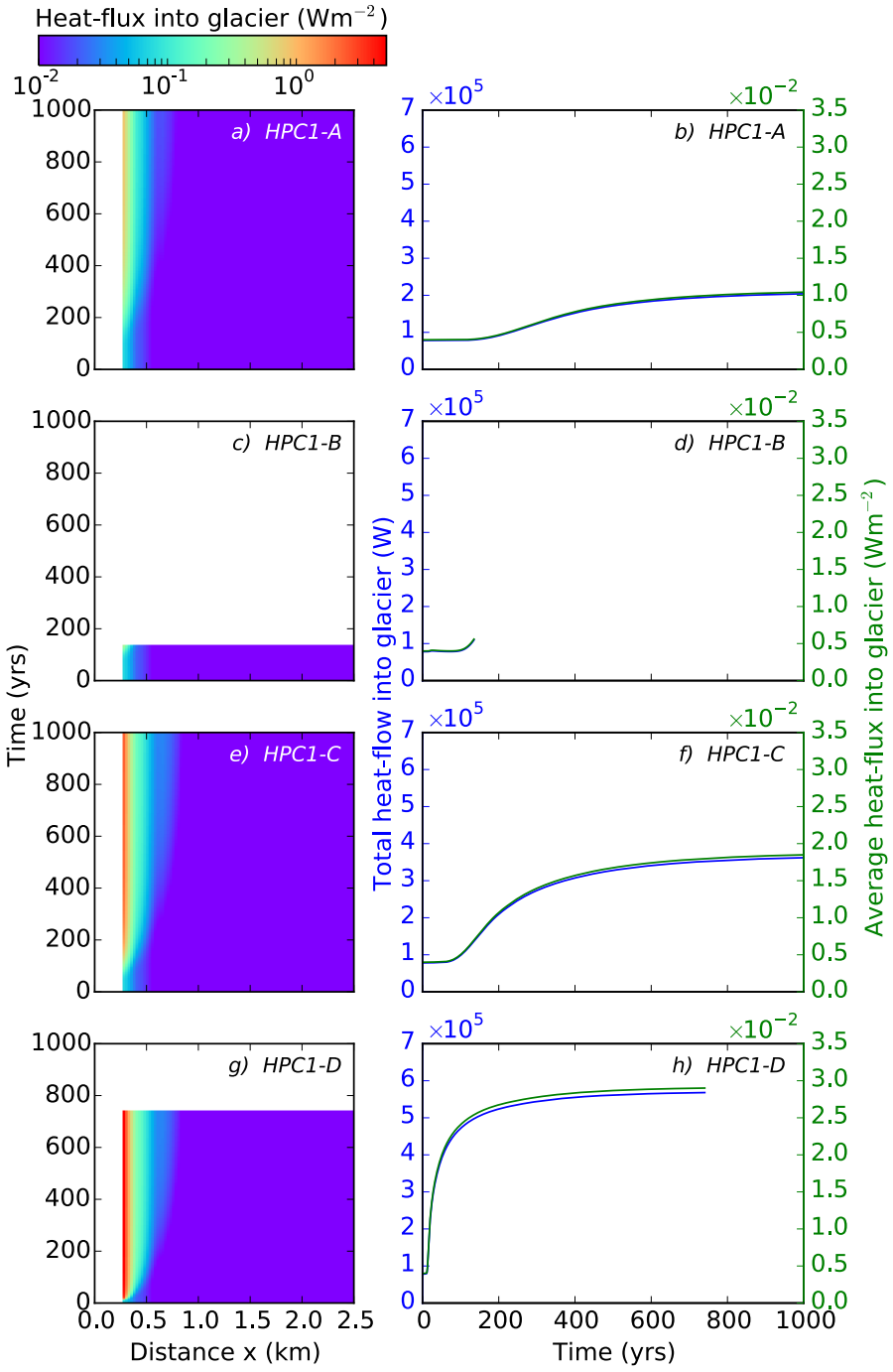

Figure A.1: *HPC1* perturbation results for the full 1000 years of perturbation. Left-hand plots show temporal and spatial variation in heat flux into glacier ($250 < x < 2500$). Right-hand plots show time series of total heat flow and average heat flux to glacier.

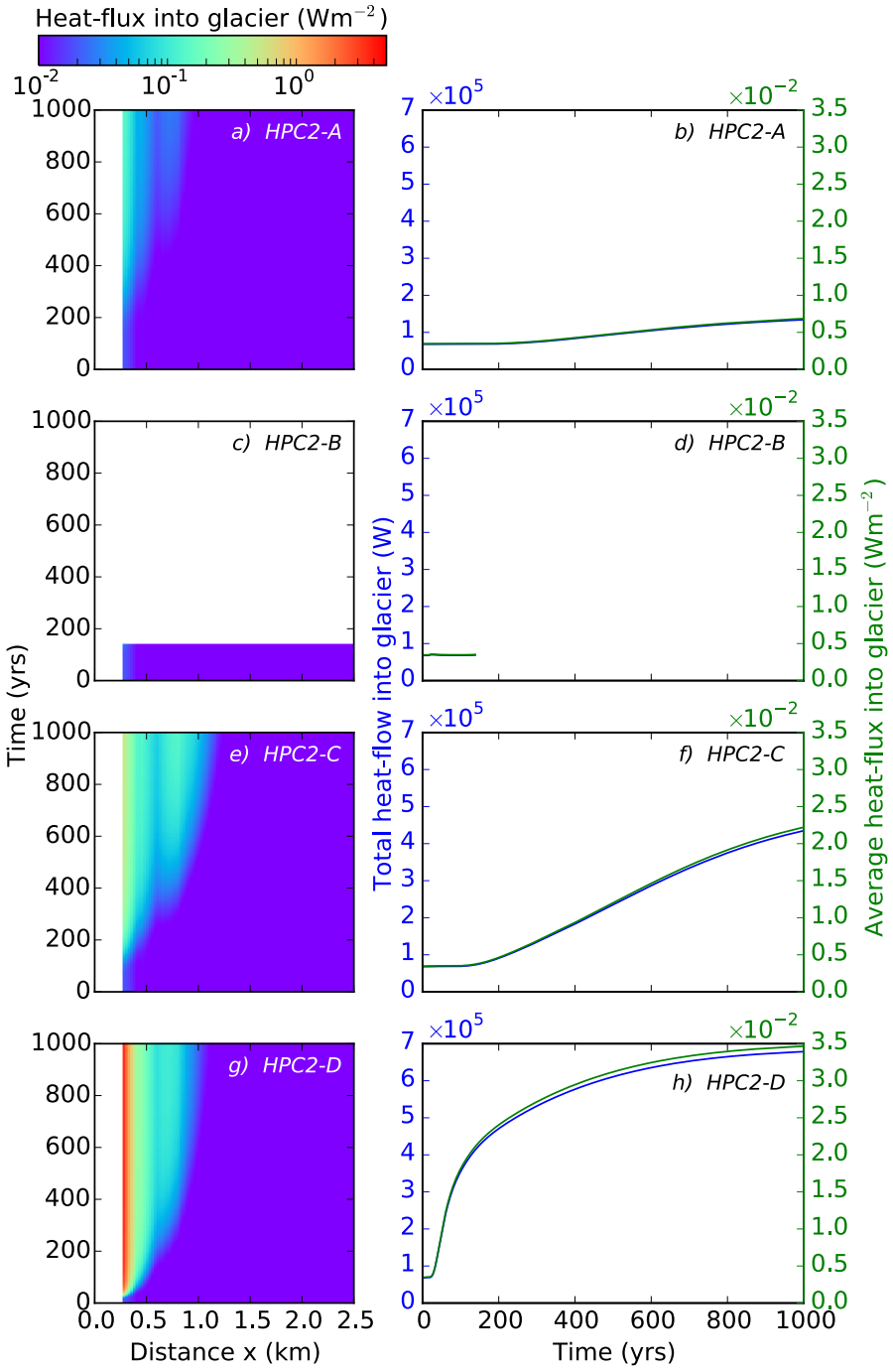

Figure A.2: *HPC2* perturbation results for the full 1000 years of perturbation. Left-hand plots show temporal and spatial variation in heat flux into glacier ($250 < x < 2500$). Right-hand plots show time series of total heat flow and average heat flux to glacier.

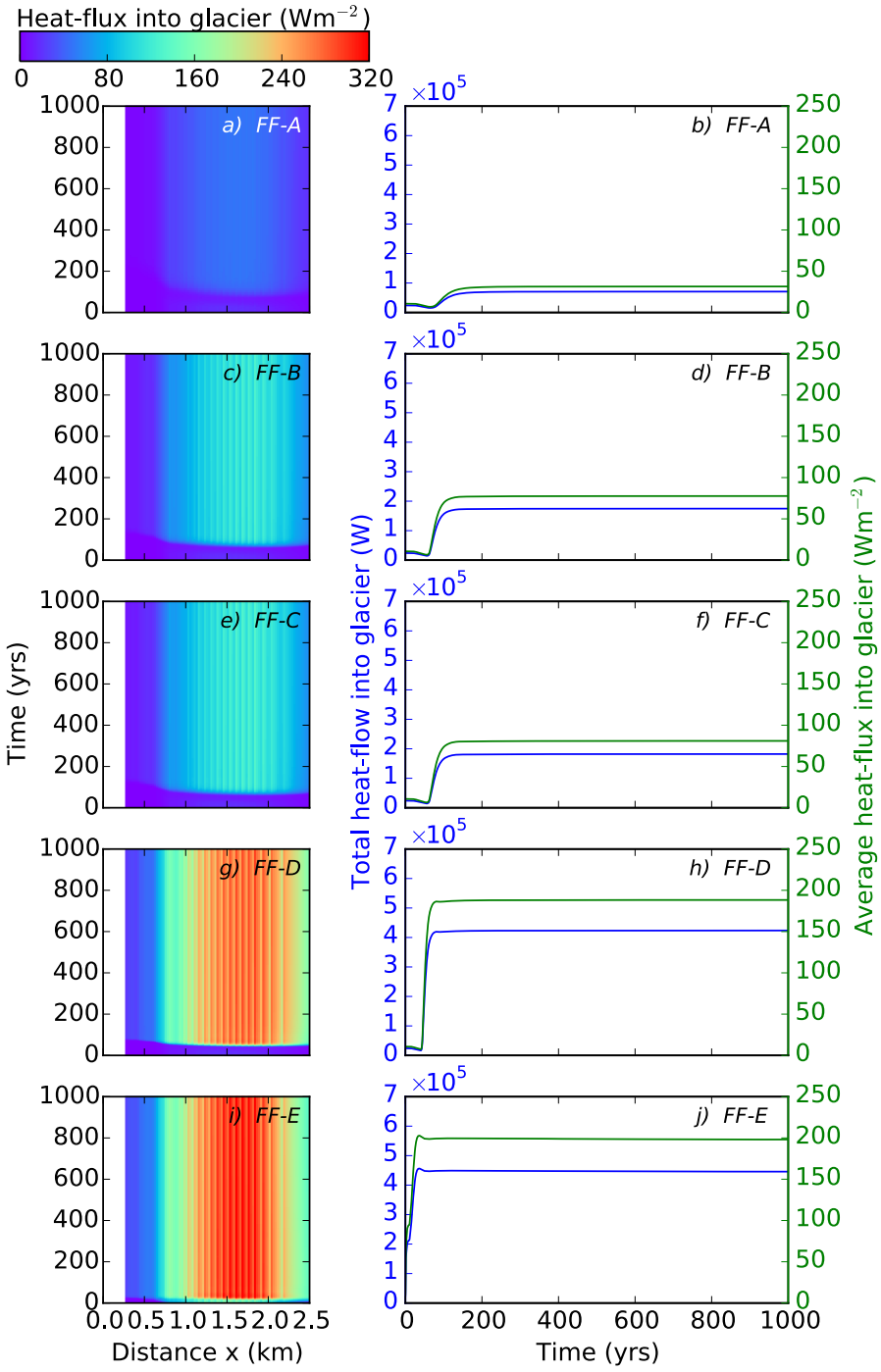

Figure A.3: *FF* perturbation results for the full 1000 years of perturbation. Left-hand plots show temporal and spatial variation in heat flux into glacier ($250 < x < 2500$). Right-hand plots show time series of total heat flow and average heat flux to glacier.

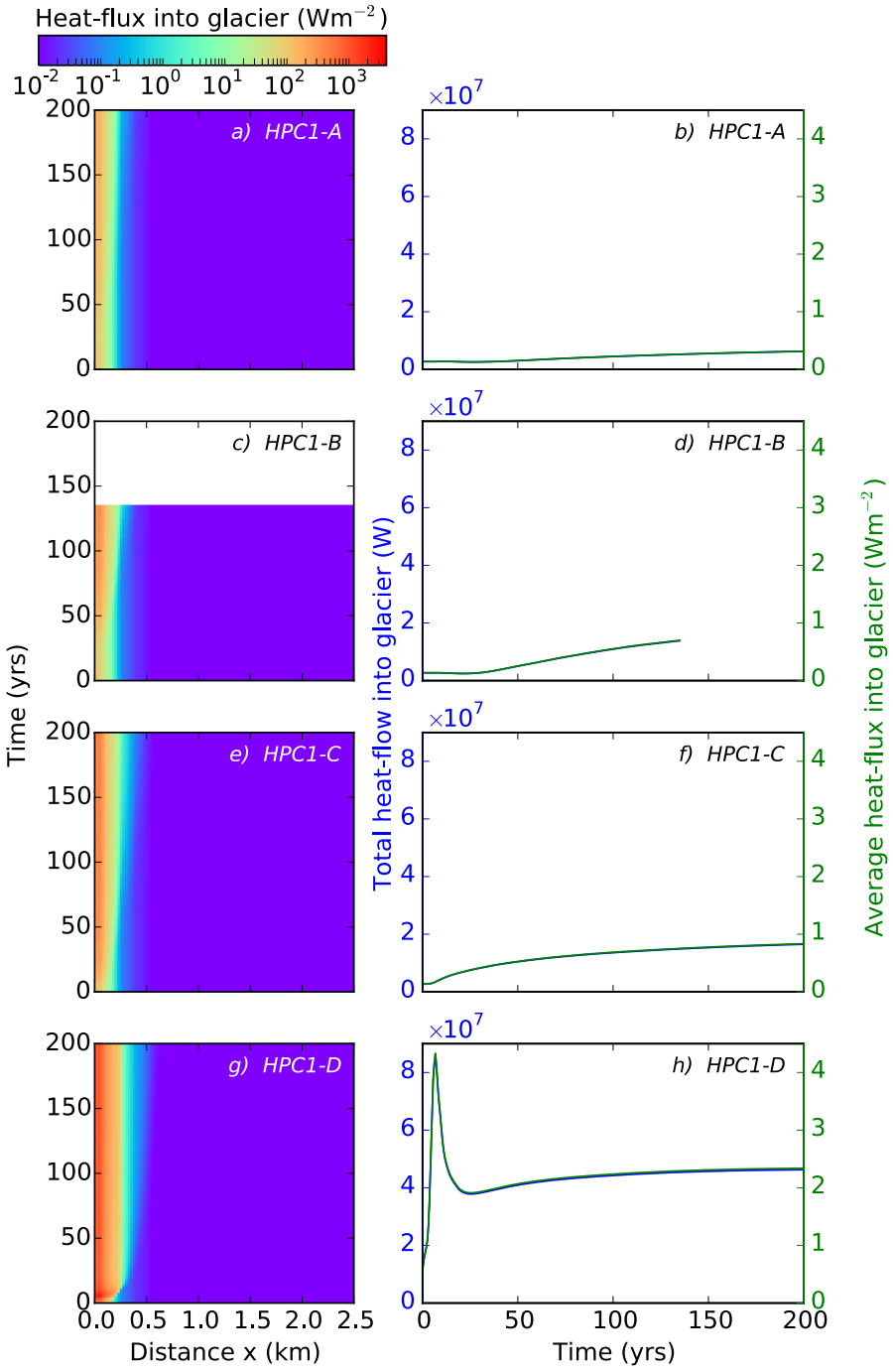

Figure A.4: *HPC1* perturbation results for the first 200 years of perturbation. Left-hand plots show temporal and spatial variation in combined heat flux into crater and glacier region ($0 < x < 2500$). Right-hand plots show time series of total heat flow and average heat flux into the combined crater and glacier regions. Note scale changes compared to Figure 7.

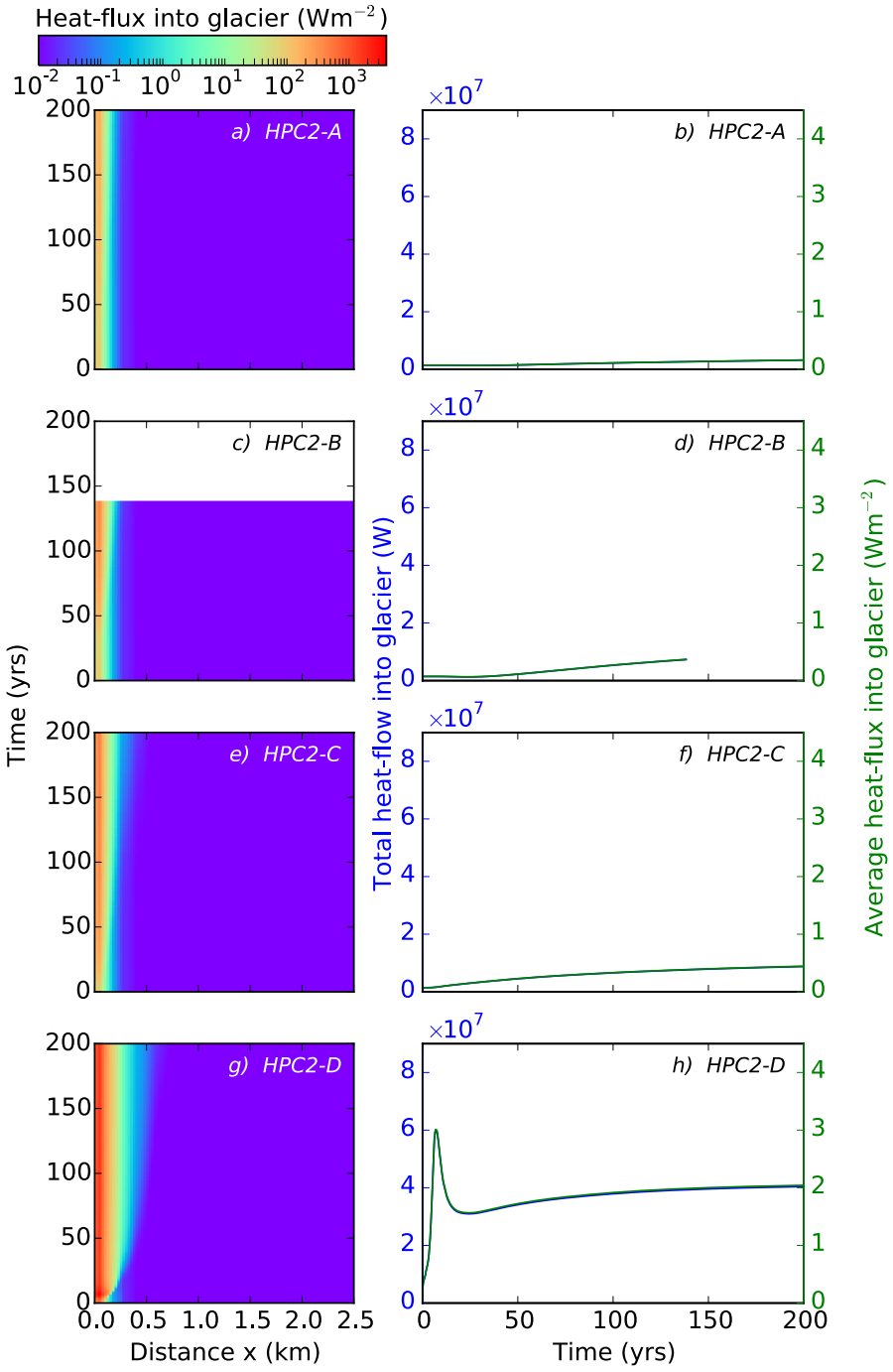

Figure A.5: *HPC2* perturbation results for the first 200 years of perturbation. Left-hand plots show temporal and spatial variation in combined heat flux into crater and glacier region ($0 < x < 2500$). Right-hand plots show time series of total heat flow and average heat flux into the combined crater and glacier regions. Note scale changes compared to Figure 8.

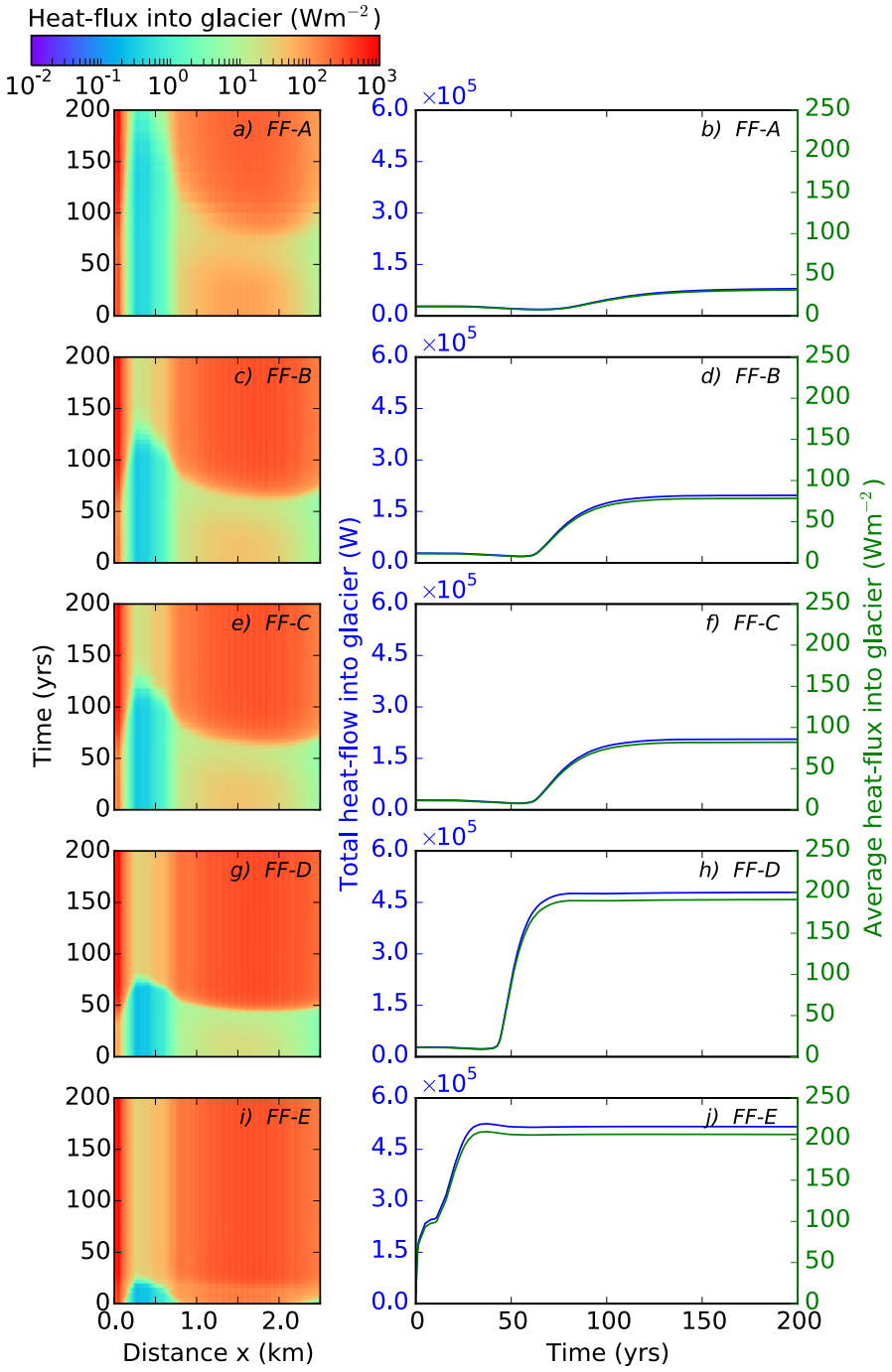

Figure A.6: *FF* perturbation results for the first 200 years of perturbation. Left-hand plots show temporal and spatial variation in combined heat flux into crater and glacier region ($0 < x < 2500$). Right-hand plots show time series of total heat flow and average heat flux into the combined crater and glacier regions. Note scale changes compared to Figure 9 and Figures A.4 and A.5.